HOCHSCHULE NORDHAUSEN
University of Applied Sciences

DLR Deutsches Zentrum
für Luft- und Raumfahrt

Department Engineering

- Energy Systems -

Numerical calculation of a Direct Steam Generating Receiver for High temperature Electrolysis

Submitted in partial fulfillment for the degree of

Master of Engineering (M.Eng.)

by

Sophia Mascher

Supervisor: *Prof. Dr.-Ing. Frank Wiese, Hochschule Nordhausen*

Co-Supervisor: *M.Sc. Timo Roeder, Deutsches Zentrum für Luft- und Raumfahrt*

Erfurt, den 27.08.2021

Vertraulichkeitsstatus

Die vorliegende Masterarbeit mit dem Thema:

„Numerical calculation of a Direct Steam Generating Receiver for High temperature Electrolysis"

Abgabedatum	27.08.2021
vorgelegt von	Sophia Mascher
betreuendes Unternehmen	Deutsches Zentrum für Luft- und Raumfahrt (DLR)
	Institut für Future Fuels
	Köln-Porz
	Nathalie Monnerie
betreuender Professor	Prof. Dr.-Ing. Frank Wiese

beinhaltet vertrauliche Informationen. Die Weitergabe des Inhalts der Arbeit und eventuell beiliegender Zeichnungen und Daten im Gesamten oder in Teilen ist grundsätzlich untersagt. Es dürfen keinerlei Kopien oder Abschriften – auch nicht in digitaler Form – gefertigt werden.

Abstract

High temperature electrolysis is an efficient solution for hydrogen production with the highest electrical efficiency. At the Deutsches Zentrum für Luft- und Raumfahrt (DLR) in Cologne a solar-driven high- temperature electrolysis (HTE) for hydrogen generation is developed. HTE typically operates at temperatures between 700-900 °C. The fed material, steam and gas, is supplied via a direct steam generating solar receiver (DSG). Upscaled HTE of 50 kWe needs temperatures above 800 °C for thermoneutral operation. However, the former receiver developed at DLR can only produce temperatures up to 700 °C. In this thesis a solar steam generator for working temperatures at 800 °C should be developed. A further novelty of this receiver is the simultaneous production of superheated steam and air. So far, DLR just developed receiver which are only considering the direct steam generation, though both steam and air are needed for HTE.

The aim of the thesis is: i) the modelling of two different cavity receiver designs, ii) evaluating efficiency and investigating the best performing receiver. The absorber tubes should in parallel evaporate and overheat water and preheat air. The design of the first concept, the FUTURE FUELS- Receiver, utilizes a helical absorber tube and the second, the SOHTEK- Receiver, utilizes multiple connected straight absorber tubes. To evaluate the DSG efficiency Lin et al. [2] approach of a 1D two-phase model of the absorber tubes, coupled to a 3D (conduction, convection, radiation) heat transfer model of the cavity and the fluid flow using Ansys Steady state thermal, should be used. Both receivers are compared in their performance and their scalability.

Table of content

I Nomenclature

Latin symbols

Symbol	Explanation	Unit
A	Area	$[m^2]$
a	Absorptivity	[-]
B	Geometry factor	[-]
Bo	Boiling number	[-]
b	Distance between both surfaces	[m]
c_p	Specific heat capacity	[J/kg K]
D	Helix coil diameter	[m]
De	Dean number	[-]
DNI	Direct normal irradiation	$[W/m^2]$
d	Diameter	[m]
E	Energy	[J]
F	Correction factor	[-]
Fr	Fraud number	[-]
G	Mass flux	$[kg/m^2 s]$
g	Gravitational constant	$[m/s^2]$
H	Enthalpy	$[kg/m^2 s]$
h	Heat transfer coefficient	[W/m²K]
k	Kinetic energy	[J]
L	Length	[m]
$\dot{m}$	Massflow	[kg/s]
N	Number	[-]
Nu	Nusselt number	[-]
P	Pipe friction coefficient	[-]
Pr	Prandtl number	[-]
p	Pressure	[bar]
Q	Power	[W]
$\dot{q}$	Heat flux density (W/m²)	[W/m²]
R	Reflectivity	[-]
Ra	Rayleigh number	[-]
r	Radius	[m]
S	Correction factors	[-]
s	Pitch	[m]
T	Temperature	[°C]
t	Time	[s]
v	Velocity	[m/s]
We	Weber number	[-]
X	Geometric factor	[bar]
X_{tt}	Martinelli parameter	[-]
x	Steam quality	[-]

Greek symbols

Symbol	Explanation	Unit
β	Thermal expansion coefficient	[1/K]
γ	Surface tension	[N/m]
ε	Emissivity	[-]
η	Efficiency	[-]
λ	Thermal conductivity	[W/m²]
μ	Dynamic viscosity	[Pa s]
ν	Kinematic viscosity	[m²/s]
ρ	Density	[kg/m²]
σ	Stefan Boltzmann constant	[W/m²K⁴]
τ	Transmittivity	[-]
φ	Constant for natural convection	[-]
φ	Geometric factor	[-]
ψ	Constant for natural convection	[-]

Subscripts

Symbol	Explanation
amb	Ambient
ap	Aperture
ave	Average
b	Boiling
C	Coil
CSP	Concentrating solar power
conv	Convection
crit	Critical
D	Solar radiation
Dry	Post dryout region
Eff	Effective
Evap	Evaporation
F	Fluid
g	Gas
h	Enthalpy
In	Inlet
Irr	Irradiation
i	Inner
LM	Logarithmic
l	Liquid
lam	laminar
lof	Liquid water only, nucleate boiling and forced convection
m	Middle
Op	optical
Out	Outlet
ph	Single-phase
R	Receiver
up	Upwind

Symbol	Explanation
rad	Radiation
re-rad	Reradiation
Sat	Saturation
St	Straight tube
sc	Subcooled
th	thermal
turb	turbulent
v	Vapor
W	Wall
2ph	Two-phase

II List of figures

III List of tables

1 Introduction

High temperature electrolysis is an efficient solution for hydrogen production with a high electrical efficiency. By providing high temperature heat to the anode and cathode of the HTE as overheated steam and gas, the required electrical energy can be minimized. Furthermore, HTE needs heat above 700 °C for thermoneutral operation, e. g. no additional heat supply is required. The target thermoneutral operation parameters for an investigated 50 kWe HTE are as followed:

Table 1: Parameters for HTE.

Process	Steam Flow	Sweep Gas Flow
Temperature	820 °C	850 °C
Mass Flow	20 kg/h	80 kg/h
Pressure	1 bar	1 bar

Current direct steam generating receiver can overheat steam up to 700 °C, see results of Future Fuels [1]. To reach a new milestone in DSG technologies an exit steam temperature of 800 °C is targeted. Furthermore, a pressure fluctuation during the evaporation of steam within the receiver is problematic for the HTE operation. Hence, a steam accumulator has to be integrated. Previous results showed that accumulate overheated steam is difficult and enormous energy losses will occur. The steam accumulator will be used, so water evaporation and superheating steam will be separated in this investigation.

This work focuses on the design of a novelty DSG concept, that can provide outlet temperatures of 800 °C and produce superheated steam and air simultaneously. For this purpose, a numerical calculation in Ansys was used to evaluate the performance of two cavity receiver designs.

2 Literature review

The direct steam generating receiver is used to provide superheated air and steam to a HTE producing hydrogen. In this chapter, HTE is at first explained. Then a summary of different receiver designs developed at DLR is presented to highlight the aspects of the existing technologies. The summary includes specific information regarding receivers that are in use and its impact on the efficiency. Next an overview of the physical aspects that govern the performance of solar receivers is given. Followed by a brief introduction on how the performance of solar receivers can be evaluated.

2.1 High Temperature electrolysis

HTE utilizes heat and electricity to decompose water steam (H_2O) into oxygen (O_2) and hydrogen (H_2) gas in the reverse mode of a solid oxide fuel cell, according to the following equation.

$$H_2O \rightarrow H_2 + \frac{1}{2}O_2 \tag{2-1}$$

HTE operates at temperatures up to 900 °C, which decreases the electricity demand compared to conventional water electrolysis, because more energy is supplied as heat instead of electricity. The electrolysis cell consists of electrolyte, the anode and the cathode, which are attached to the electrolyte at the opposite sites. Water steam is supplied to the cathode, where it is decomposed into hydrogen and oxygen ions. To start the splitting process, electric energy is supplied. The hydrogen is removed as the end product and oxygen moves to the anode through the electrolyte that is conductive for oxygen ions. At the anode, the oxygen ions are oxidized and recovered as oxygen. [3]

The receiver investigated in this thesis, is based on the following HTE system configuration (Figure 1).
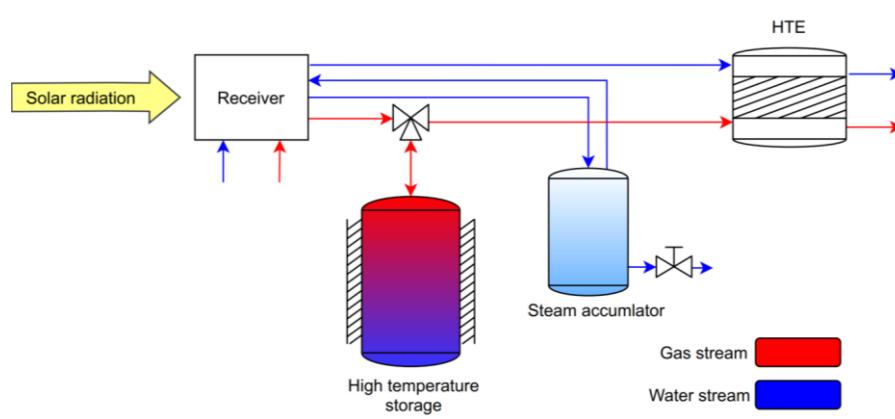
Figure 1: Solar assisted HTE process scheme.

Concentrated solar radiation is used to evaporate water and superheat air and steam in a receiver. The steam is then supplied to a steam accumulator, to compensate the pressure difference and to separate the remaining water liquid from the steam. The heated gas stream not only supplies the energy to the HTE, it also charges a high temperature thermal energy storage. The storage is used for continuous operation during cloud shading and also helps during the starting phase of the process. Both heated gas and steam are needed for operating a HTE.

2.2 Previous concepts

As the partner of the European funded SOPHIA project (solar integrated pressurized high temperature electrolysis) the DLR developed a solar driven HTE process. The solid oxide electrolysis cell (SOEC) is driven at a steam temperature of 750 °C and 15 bars. As part of this project, a few receiver designs were developed. The first one was a solar tube type receiver with cylindrical configuration of 20 absorber tubes of high alloy steel. The feeding mass flow was set to 5 kg/h at 700 °C outlet temperature. The development of the solar tube-type receiver was carried out using the engineering equation solver EES and the ray tracing tool OptiCAD. The tube diameter was set to standard size for tube type receiver. The number of tubes was set to shape the cavity, whose diameter was determined by the focal point of DLR's solar simulator. In a parametric study the tube length was solved according to the integral heat balance of the system, considering the solar irradiation, the energy needed to superheat steam, as well as the convective and conductive heat losses. Furthermore, to determine the heat flux and to locate hot spots the tubes have been discretized to calculate both radiative and convective heat losses. In a raytracing simulation a hotspot in the center of the cavity was detected due to the offset of

the focus. For this purpose, the receiver was positioned 60 mm behind the focus. In a test campaign the receiver was tested in the solar simulator of DLR in Cologne. The first campaign showed the operability with nitrogen and the following campaigns with water steam. Furthermore, in the third campaign a water-cooled cover was installed to reduce spillage of the solar radiation and implicitly the heating of the housing. During the experiments the mass flow and the incoming heat flux were varied (Figure 2). [4]
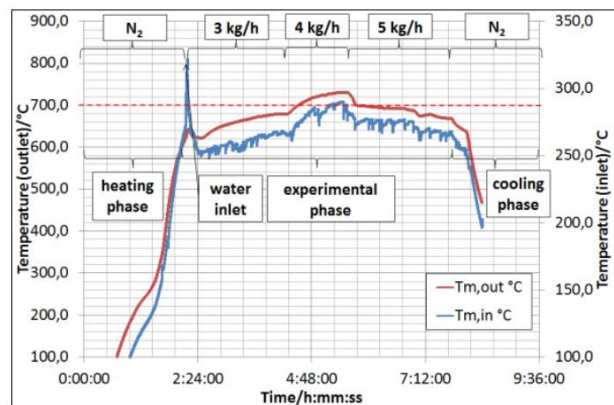
Figure 2: Experimental analysis receiver 1 Sophia project [4].

They reached output temperatures of 700 °C at 90 % shutter opening[1] and a mass flow of 3 kg/h. At 4 kg/h and 100 % shutter opening they reached outlet temperatures of 720 °C. When they increased the mass flow to 5 kg/h and 100 % shutter opening the temperature dropped to 700 °C. The receiver reached a thermal efficiency of 40 % at 5 kg/h and a solar power input of 4 kW. The main problem of the solar receiver was the fluctuating mass flow as well as the temperature. The major challenge of the multi-tubular receiver was the uniformity of the vapor distribution on the 20 tube to ensure an identical mass flow and heat transfer on every tube. For this purpose, a distribution system was developed. The receiver was tested for a mass flow up to 10 kg/h of steam generation from 1 to 3 bar at 750 °C. The problem for water boiling was the lack of homogenous water distribution for the different tubes compared with steam flow which causes instability. To tackle this, a distribution system was developed.

---

[1] Shutter opening refers to how far the shutter of the Synlight test chamber, in which the solar radiation is concentrated, is open.

The second design was the receiver with a modified steam distribution system. The steam was again superheated to 700 °C. The system capacity was at 10 kg/h steam and the experiment was carried out for pressure between 1 and 3 bar at 750 °C (Figure 3).
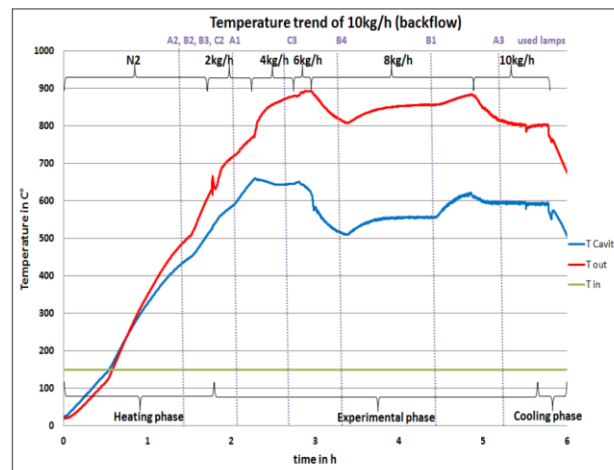
Figure 3: Experimental analysis receiver 2 Sophia project [5].

They discovered weaknesses in water boiling. The lack of homogenous water distribution for the different tubes compared with steam flow causes challenges in stability. For this reason, a new receiver design was developed. [5]

To improve the design of receiver 2, a comparison of two designs was carried out. A validated numerical model was developed to couple 3D heat transfer (conduction, convection, radiation) of the cavity with a 1D two-phase flow inside the absorber tubes to evaluate the performance of the receiver. Two different receiver designs, a helical absorber and straight, connected absorber tubes and the impact of the fluid flow rate, pressure, surface emissivity, inlet position, tube diameter, helical shape and the water-cooled receiver front were investigated (Figure 4).
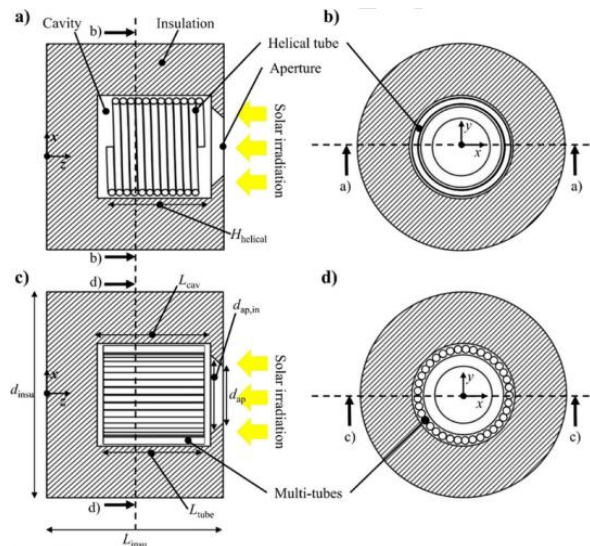
Figure 4: Spiral (a) and (b), cylindrical receiver 2 (c) and (d) [2].

The spiral receiver exhibited larger re-radiation heat losses and smaller conductive and convective heat losses compared to the cylindrical receiver at large solar power (10 kW in the study). Furthermore, the solar-to-thermal efficiency for the spiral was always higher than the cylindrical. They investigated a significant effect of the flow rate on the solar-to-thermal efficiency. The efficiency increased with increasing flow rate for spiral receiver until the curve flattens at 0.55 g/s under reference conditions. The cylindrical receiver showed an increased efficiency at a smaller flow rate than 1 g/s. Furthermore, the receiver could achieve higher solar-to-thermal efficiency, compared to the spiral receiver, when the tube's emissivity was smaller than 0.58. The spiral receiver was more sensitive to the variation in pressure than the cylindrical receiver but the solar-to-thermal efficiency decreases with increasing inlet fluid pressure. Under reference conditions, they examined a pressure region between 10-15 bar where the decrease in efficiency was more prominent. For spiral receiver, the fluid inlet position played an important role. The front inlet was recommended when conductive and convective heat losses dominate (at small solar power (1.5 kW)) and the back when radiation dominates (at high solar power (10 kW)). Furthermore, they investigated a correlation between the tube diameter and the efficiency. Spiral Receiver showed better efficiency at a smaller diameter than 7.5 mm and cylindrical at larger diameter than 7.5 mm, due to the smaller re-radiation for cylindrical receiver. The reference shape of the helical tube (cylindrical) exhibited a higher solar-to-thermal efficiency than conical shape of the helical tube. The cylindrical receiver showed a significant reduction in efficiency resulting from very high re-radiation losses, which increased with increasing solar power-input. The water-cooled front was added to remove the spillage irradiation heating the receiver front. This led to higher conductive heat losses and thereby decreased the solar-to-thermal efficiency by 0.5-1.5 %. The authors suggested increasing the

solar power input to reduce the decrease in efficiency. Because the steam in the spiral receiver flows through one tube, mass flow fluctuations can be avoided (which lead to pressure and temperature fluctuations) and thereby, the overall performance was comparatively better than the cylindrical. It was deemed to be the most suitable technology for the integration to the process of hydrogen production stack. The test campaign showed that 5 kg/h steam mass flow at 800 °C from 20 °C water could be reached. The challenge with this receiver was the pressure surge of the stack which needed further optimization to solve this problem.

The receiver 3 was further optimized with an additional inner reflector cone to provide better heat flux distribution on the spiral absorber. Thereby steam and mass flow fluctuations which can lead to pressure and temperature fluctuations should be avoided. The experiment showed that the aspired steam temperature of 800 °C were reached up to a steam mass flow of 5 kg/h at 20 °C input temperature. The receiver has been further adapted to distribute the heat flux on the absorber tubes more evenly by adding an inner reflector cone more evenly (receiver 4) (Figure 5).
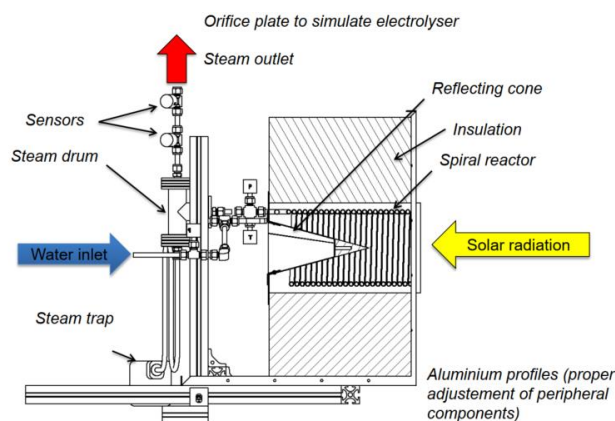
Figure 5: Receiver concept 4 of the Sohtek receiver [5].

The mass flow was set to 2 kg/h which lead to an outlet temperature of 370 °C. The temperatures were steady and the pressure stayed within the limits of 45 mbar. Because the receiver setup 4 delivered steady state results, it was the base for further and final optimization. The receiver has been insulated better and a steam accumulator was added. The final test showed a capacity of 5 kg/h of steam generation at 700 °C. The new regulation system allowed a regulation of the mass flow between 0.5 and 5 kg/h without big fluctuations. As outlook they planed further simulations of clouds to investigate the behavior of the overall system.

The receiver was further developed in the project "Future Fuels" as a conical spiral solar steam generator made from high temperature stainless steel grade 1.4841, 10 mm inner tube diameter and 1.5 mm thickness. The conical shape should improve the heat flux distribution on the absorber tubes. The spiral tube was insulated with a housing ("PROMAFORM 1600") to prevent heat losses and to hold the cavity in place. The first campaign was done with 3 lamps irradiating the receiver with 5.66 kW (0.0201m² and 160 mm aperture diameter) which leads to an average flux of 282 kW/m² and produces a steam mass flow of 5 kg/h. [6]. The receiver was then constructed and tested under the solar simulator at DLR in cologne. To avoid pressure and mass flow fluctuations to the water pump and the flow controller, they did use a reserve water tank. The water level is maintained at a constant level, i.e. 5 kg/h water flow. A pressure booster was used to provide the inlet pressure at the desired level. The superheated steam was then fed into a steam accumulator for storage to avoid fluctuations in temperature, pressure and steam supply. The vessel was designed with a volume of 33 l, a maximum temperature of 400 °C and pressure of 25 bars. Because heat losses occurred both in the steam accumulator and the connection tube from the steam generator to the accumulator, the steam accumulator was located 100 cm away from the steam generator. They also said, that both problems could be optimized by rearranging the two components as close as possible and by improving the insulation of the connection tubes. In the first test phase, the heating phase, the steam output ranged from 4.7-5.3 kg/h. The receiver showed a highly dynamic behavior, rapidly increasing the steam outlet temperature from 25 °C to 470 °C. The overall average outlet temperature was in the range of 450 °C. They furthermore investigated, that during a cloud formation (simulated by switching off both the solar simulator and the water/steam flow) the accumulator showed a lower temperature decrease than the steam generator. The steam generator temperature decreased drastically. Within 1 h after the interruption the steam generator temperature did rise to the evaporation temperature of the present pressure and rises with pressure until nearly constant. This indicates that during the whole operation process liquid water is present in the steam accumulator. This again underlines the function of the accumulator for buffering fluctuations in solar radiation supply [7].

2.3 Conjugate heat transfer

Solar receiver highly depend on their ability to capture and transfer solar radiation to the fluid. The transport of thermal energy or heat occurs by three mechanisms: conduction, convection and radiation.

In the case of this thesis, the following heat transfer ways are considered for the point-focus concentrated solar collectors:

- Natural convection
- Internal forced convection
- Internal and external radiation and re-radiation

2.3.1 Natural convection

Natural convection happens because of the temperature gradient between the ambient with 298 K and the outer surface of the cavity as well as the inner cavity wall and the cavity itself. In this case, according to Lin et al. [2] the heat transfer coefficient for the natural convection from the outer wall of the insulation was set to 5 W/m²K. The heat transfer coefficient for the inner cavity wall was calculated according to Paitoonsurikarn et al. [8] where the Nusselt number Nu for free convection in various geometries can be calculated according to

$$Nu = 0.0196 Ra^{0.41} Pr^{0.13} \qquad (2\text{-}2)$$

where Ra is the Rayleigh number

$$Ra = \frac{g\beta(T_{\mathrm{w}} - T_{\mathrm{amb}})L^3}{\nu\alpha} \qquad (2\text{-}3)$$

The Prandtl number Pr is defined as

$$Pr = \frac{\nu}{\alpha} \qquad (2\text{-}4)$$

g is the gravitational constant, β is the thermal expansion, L is the relevant scale, ν is the kinematic viscosity and α is the thermal diffusivity of air. All values refer the film temperature which is the average between the wall and the ambient temperature, T_{w} and T_{amb}.

The dimensional length in Eq. (2-2) describes the ensemble cavity length by considering the cavity geometry and inclination. It can be evaluated as:

$$L = \left| \sum_{i=1}^{3} a_i cos(\phi + \psi_i)^{b_i} L_i \right| \tag{2-5}$$

L_i is the cavity length, a_i, b_i, ϕ and ψ_i are constants which are summarized in Table 2.

Table 2: Constant values for free convection. [8]

i	a_i	b_i	ψ_i
1	4.08	5.41	-0.11
2	-1.17	7.17	-0.3
3	0.07	1.99	-0.08

2.3.2 Internal forced convection

For solar receivers the critical aspect is the heat transfer of the absorbed heat flux for use in power generation. If the heat transferred $\dot{q}_{conv}$ is uniformly distributed on the absorber tube surface, the heat transfer to the fluid can be calculated according to Newtons Law of Cooling.

$$\dot{q}_{conv} = h(T_W - T_F) \tag{2-6}$$

Respectively

$$\dot{Q}_{conv} = A_{tube} h \Delta T_{LM} \tag{2-7}$$

Here, A_{tube} is the inner surface area of the tube and ΔT_{LM} is the average logarithm temperature of the fluid and can be expressed as

$$\Delta T_{LM} = \frac{(T_W - T_{in}) - (T_W - T_{out})}{ln\left(\frac{T_W - T_{in}}{T_W - T_{out}}\right)} \tag{2-8}$$

with T_{Fluid} as the fluid temperatures and h as the heat transfer coefficient which is derived using the Nusselt number Nu, the inner diameter d_i and the thermal conductivity λ.

$$h = Nu \frac{\lambda}{d_i} \tag{2-9}$$

It should be mentioned, that the heat flux on the absorber surface in solar receiver is rarely uniformly distributed. For now, a uniform distributed heat flux is considered.

2.3.3 Internal and external radiation and re-radiation effects

Radiation occurs in all directions from bodies with a temperature above zero Kelvin. The distribution of the rays depends on the surface. The ideal body, a blackbody, emits and absorbs all radiation perfectly diffusively and is used as a standard to which real surfaces are compared. Real surfaces are collectively known as grey surfaces and have an average emissivity value which is lower than the blackbody ones and cannot achieve perfect diffusivity.

The incoming electromagnet wave, known as the solar irradiation, is to a certain fraction absorbed, reflected or transmitted by the surface of a body dependent on the properties of the body. The percentage depends on the absorptivity a, reflectivity R and the transmissivity τ, if the body is semi-transparent and can be calculated with

$$a + R + \tau = 1 \qquad (2\text{-}10)$$

These factors are a function of the wavelength of the incoming light and the angle of the irradiance.

2.3.4 Heat transfer enhancement

Enhancing the heat transfer will lead to an improved overall energy efficiency and reduction in size and cost of the system. Possible techniques for heat transfer enhancement can be classified as active, passive and compound techniques. The active techniques include external power, while the passive one doesn't and the compound combines both techniques (see Table 3).

Table 3: Classification of Heat transfer enhancement techniques.

Passive Techniques	Active Techniques	Compound Techniques
Treated Surfaces	Mechanical Aids	Two or more active and passive
Rough Surfaces	Surface Vibration	techniques that are employed
Extended Surfaces	Fluid Vibration	together.
Displaced Enhancement Devices	Electrostatic Fields	
Swirl Flow Devices	Injection	
Coiled Tubes	Suction	
Surface Tension Devices	Jet Impingement	
Additive for Liquids		
Additives for Gases		

Because of the absence of moving components and auxiliary power, passive techniques have higher reliability then active techniques. For enhancing boiling heat transfer mainly working fluids and solid surfaces are modified. In many cases it is not possible to modify the working fluid, due to restrictions which arise from applications such as steam generation cycles. In such cases, micro-nano scale surface enhancement through surface roughening or surface coating techniques can be used for altering the surface parameters, dependent on the optimization condition of the application.

The view factor in radiative heat transfer can furthermore be utilized to maximize the absorbed solar irradiation. Certain materials and coatings such as

- Increasing the absorptivity of an absorber tube with a high-temperature paint
- Increasing reflectivity of a cavity's insulating walls by making use of thin mirrors or polymer films
- Optical coatings that reflect certain wavelength of electromagnetic waves

can be used to maximize the cavity receiver's efficiency.

2.4 Performance definition

The performance of solar receiver can be described as the ability to transform energy as effectively as possible. The efficiency can be separated into optical and thermal efficiency. The optical efficiency is briefly introduced for heliostat fields. The pressure drop is also relevant for evaluating the best performing receiver, as it is influencing the heat transfer coefficient.

2.4.1 Optical efficiency

The optical efficiency determines the amount of energy available from the light source compared to how much energy is passed to a solar collector. Material, as well as environmental factors and the geometry affect the solar field performance. In the case of point-focus systems, the optical efficiency can be quantified by

$$\eta_{CSP,op} = \frac{A_{ap} \int \dot{q}_{rad}}{DNI \sum A_{heliostat}} \qquad (2\text{-}11)$$

for CSP towers.

DNI determines the direct normal irradiation. The subscripts ap and heliostat refer the aperture and heliostat area. This efficiency only applies to a solar field.

2.4.2 Thermal efficiency

The thermal efficiency of the solar receiver η_{th} compares the incoming solar radiative power with the generated receiver power.

$$\eta_{th} = \frac{E_R}{E_D} = \frac{\dot{m}(H_{out} - H_{in})}{\dot{q}_{sol} \, A_{tube}} \qquad (2\text{-}12)$$

The parameter E_R corresponds to the receiver power, E_D the solar radiation power, H the enthalpy and $\dot{q}_{sol}$ the heat flux density.

2.4.3 Pressure drop

Single-phase frictional pressure drop

According to Bernoulli's principle, the velocity increases with decreasing pressure. Because the velocity affects the heat transfer, the pressure drop in the absorber tubes is relevant for the receiver's performance. It is assumed that the absorber tube has a smooth surface. Blasius equation as shown below was used to calculate the pipe friction coefficient P[9].

$$P = 0.3164 Re^{-1/4} \qquad (2\text{-}13)$$

Here, Re is the Reynolds number of the fluid. The pressure drop is calculated by using the following equation.

$$\Delta p = P \frac{L}{d} \frac{1}{2} \rho v^2 \qquad (2\text{-}14)$$

Two-phase frictional pressure drop

Zhao's correlation [10] was used to calculate the frictional pressure drop in the two-phase flow. The correlation is expressed as follows,

$$\Delta p_{2\text{ph}} = \emptyset_l^2 \Delta P_l \qquad (2\text{-}15)$$

$\Delta p_{2\text{ph}}$ is the two-phase flow frictional pressure drop, ΔP_l is the single-phase frictional pressure drop at the same mass flux when the fluid is entirely liquid, and $\emptyset_l^2$ is the two-phase frictional multiplier. The two-phase frictional multiplier from Zhao's correlation was modified and the following equation was used to calculate the two-phase frictional multiplier in the validation.

$$\emptyset_l^2 = 1 + \left(\frac{\rho_l}{\rho_v} - 1\right)\left[0.303 x^{1.63}(1-x)^{0.885} Re_l^{0.267} + x^2\right] \qquad (2\text{-}16)$$

Zhao's correlation was chosen since the geometry and operating conditions were similar to this study. The following table shows the comparison of both studies.

Table 4: Comparison of helical tube's geometry and operating conditions between Zhao's study and our study.

Parameters	This study	Zhao [10]
Inner tube diameter, d_i [mm]	20	9
Helix coil diameter, D [mm]	250	292
Curvature ratio (d_i/D) [-]	0.0794	0.031
System pressure [MPa]	1.0	0.5 – 3.5
Heat flux [kW/m^2]	82.715	0 - 900
Mass flux [kg/m^2 s]	35.367	236 - 943
Orientation	Horizontal	Horizontal

3 Heat transfer in single-phase flow

The single-phase flow occurs when just one phase is present. In all three process steps (evaporating water, superheating steam and superheating air) the whole fluid or at least a part exists as single-phase. The following chapter describes the heat transfer in this region to determine the heat transfer coefficient as seen in Eq. (2-8) which is needed as input parameter for the Ansys simulation.

3.1 Straight tube

The local heat transfer coefficient is calculated according to VDI heat atlas [9] for laminar or turbulent flow in a tube. The Nusselt number depends on the fluid flow regime, and the tube geometry. For straight tubes, it can be expressed by the following equations.

If $Re < 2300$ (laminar flow), than,

$$Nu_m = \left\{ Nu_{m,1}^3 + 0.7^3 + \left[Nu_{m,2} - 0.7 \right]^3 + Nu_{m,3}^3 \right\}^{\frac{1}{3}} \tag{3-1}$$

$$Nu_{m,1} = 3.66 \tag{3-2}$$

$$Nu_{m,2} = 1.615 \sqrt[3]{\frac{RePrd_i}{l}} \tag{3-3}$$

$$Nu_{m,3} = \left(\frac{2}{1 + 22Pr} \right)^{1/6} (RePrd_i/l)^{1/2} \tag{3-4}$$

Since the tube length set in this study was long ($d_i/l < 0.1$), $Nu_{m,3}$ was excluded from Eq. (3-1). Therefore, the following equation was used to calculate the Nusselt number of the fluid in the laminar flow.

$$Nu_{\mathrm{m}} = \left\{ Nu_{\mathrm{m},1}^3 + 0.7^3 + \left[Nu_{\mathrm{m},2} - 0.7 \right]^3 \right\}^{\frac{1}{3}} \tag{3-5}$$

If $10^4 < Re \leq 10^6$ (fully developed turbulent flow), than,

$$Nu_{\mathrm{m}} = \frac{\left(\frac{\xi}{8} \right) RePr}{1 + 12.7 \sqrt{\frac{\xi}{8}} \left(Pr^{\frac{2}{3}} - 1 \right)} \left[1 + \left(\frac{d_{\mathrm{i}}}{l} \right)^{\frac{2}{3}} \right] \tag{3-6}$$

$$\xi = (1.8 log_{10} Re - 1.5)^{-2} \tag{3-7}$$

The range of validity of Eq. (3-6) is $0.1 \leq Pr \leq 1000$, $d_{\mathrm{i}}/l \leq 1$.

If $2300 \leq Re \leq 10^4$ (transition region), than,

$$Nu_{\mathrm{m}} = (1 - \gamma) Nu_{\mathrm{lam},2300} + \gamma Nu_{\mathrm{turb},10^4} \tag{3-8}$$

$$\gamma = \frac{Re - 2300}{10^4 - 2300} \quad (0 \leq \gamma \leq 1) \tag{3-9}$$

Here, $Nu_{\mathrm{lam},2300}$ is the Nusselt number at $Re = 2300$ calculated from Eq. (2-5) and $Nu_{\mathrm{turb},10^4}$ is the Nusselt number from Eq. (2-6) at $Re = 10^4$. The range of validity of Eq. (2-8) is $0.6 \leq Pr \leq 1000$, $d_{\mathrm{i}}/l \leq 1$.

3.2 Helical tube

In the case of a helical tube, it can be expressed as the following equations.

If $Re < Re_{\mathrm{crit}}$ (laminar flow), than,

$$Nu = 3.66 + 0.08 \left[1 + 0.8 \left(\frac{d_i}{D}\right)^{0.9}\right] Re^m Pr^{\frac{1}{3}} \left(\frac{Pr}{Pr_w}\right)^{0.14} \tag{3-10}$$

$$m = 0.5 + 0.2903 \left(\frac{d_i}{D}\right)^{0.194} \tag{3-11}$$

Here, Re_{crit} is the critical Reynolds number, Pr_w is the Prandtl number of the fluid (see Eq. (2-4), when it is at wall temperature, and D is the average diameter of the curvature of the coil. Since the secondary flow occurs at the helical tube and stabilizes the laminar flow, the transition from laminar to turbulent flow is shifted to higher Reynolds numbers. That higher Reynolds number is called "critical Reynolds number," and it is expressed as follows.

$$Re_{crit} = 2300 \left[1 + 8.6 \left(\frac{d_i}{D}\right)^{0.45}\right] \tag{3-12}$$

The average diameter of the curvature of the coil can be calculated by using the projected diameter of a winding D_c and pitch s (see Figure 6).
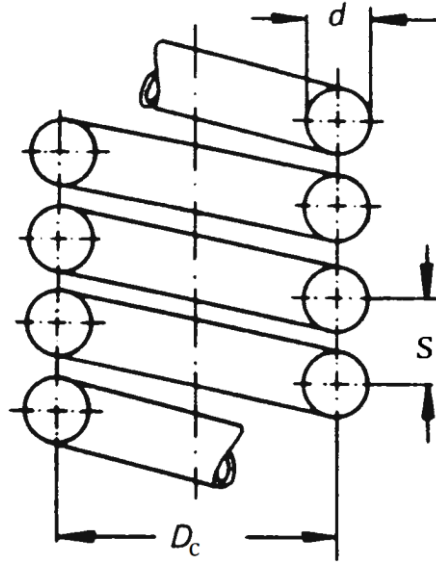
Figure 6: Geometry parameters of the helical tube. [9]

$$D = D_c \left[1 + \left(\frac{s}{\pi D_c}\right)^2\right] \tag{3-13}$$

If $Re > 2.2 \times 10^4$ (fully developed turbulent flow), than,

$$Nu = \frac{\left(\frac{\xi}{8}\right) Re Pr}{1 + 12.7 \sqrt{\frac{\xi}{8}} \left(Pr^{\frac{2}{3}} - 1\right)} \left(\frac{Pr}{Pr_{\text{rw}}}\right)^{0.14} \tag{3-14}$$

$$= \left[\frac{0.3164}{Re^{0.25}} + 0.03 \left(\frac{d_{\text{i}}}{D}\right)^{0.5}\right] \left(\frac{\mu_f}{\mu}\right)^{0.27} \tag{3-15}$$

Here, μ is the dynamic viscosity and μ_{f} is the dynamic viscosity of the fluid at wall temperature.

If $Re_{crit} < Re < 2.2 \times 10^4$ (transition region), than,

$$Nu = \gamma Nu_{\text{lam,crit}} + (1 - \gamma) Nu_{\text{turb},2.2 \times 10^4} \tag{3-16}$$

Where

$$\gamma = \frac{2.2 \times 10^4 - Re}{2.2 \times 10^4 - Re_{\text{crit}}} \quad (0 \leq \gamma \leq 1) \tag{3-17}$$

Here, $Nu_{\text{lam,crit}}$ is the Nusselt number at Re_{crit} calculated from Eq. (2-12) and $Nu_{\text{turb},2.2 \times 10^4}$ is the Nusselt number from Eq. (2-14) at $Re = 2.2 \times 10^4$.

4 Heat transfer in two-phase flow

The following chapters explain the calculation of the heat transfer coefficient for different flow regimes in the two-phase region and the wall temperature, respectively. The two-phase flow occurs in the water evaporation. At first the thermodynamics of the phase change is briefly introduced. Followed by the approach of calculating the heat transfer coefficient as seen in Eq. (2-8) which is needed as input parameter for the Ansys simulation.

In the evaporation process, different flow regimes along the tube's length according to the vapor content occur (see Figure 7).
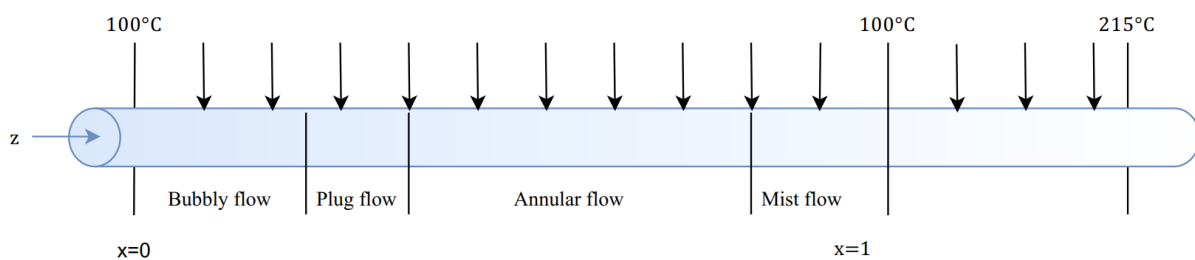
Figure 7: Heat transfer and flow regimes in the two-phase region in a horizontal tube.

In our study, the flow regime of the two-phase flow was divided mainly into three subregions; (i) a nucleate boiling dominated subregion (roughly corresponding to bubbly and plug flow), (ii) forced convection evaporation dominated subregion (roughly corresponding to stratified, stratified wavy, intermittent or slug, and annular flow), (iii) a post dryout subregion (roughly corresponding to mist flow). In the nucleate boiling subregion, heat transfer mostly occurs through nucleation and detachment of bubbles at the wall. In the forced convection evaporation subregion, there are typically no bubbles, and heat transfer occurs mainly through convection within the liquid film and evaporation at the liquid film/vapor core interface. With increasing steam quality, the heat transfer becomes forced convection dominated and the bubble formation components converges towards zero. In the post dryout subregion, the liquid film completely disappears and the heat transfer mostly occurs through convection within the vapor. Therefore, the heat transfer coefficient drops drastically and thus the tube wall temperature rises abruptly.

The thermal analysis must be divided into three phases according to the phase change starting with the single-phase water, followed by the two-phase flow and finishing with the single-phase steam.

The subcooled region L_{sc} is the length where liquid flow only occurs. It can be calculated with

$$L_{\text{sc}} = \frac{\dot{Q}_{\text{h(out-in)}}}{\dot{q} \, \pi \, d} \tag{4-1}$$

$$\dot{Q}_{\text{h(out-in)}} = \dot{m}(h_{\text{out}} - h_{\text{in}}) \tag{4-2}$$

$$\dot{Q}_{\text{evap}} = \dot{m} \, h_{\text{evap}} \tag{4-3}$$

The tube should be discretized along its length in the z-direction for the two-phase flow. At each segment the steam quality was calculated using the energy balance. [12]

$$x = \frac{\pi d_i l_i \dot{q}}{\dot{m}(h_g - h_f)} \tag{4-4}$$

The subscripts g, f and in refer to the gas, liquid phase and inlet.

The length until the vapor only phase (x=1) L_{evap} can be calculated using (3-4).

$$L_{\text{evap}} = \frac{\dot{m}(h_g - h_f)}{\pi d_i \dot{q}} \tag{4-5}$$

The same equation can be used for calculating the length for the steam only phase L_g.

$$L_g = \frac{\dot{m} \, h_g}{\pi d_i \dot{q}} \tag{4-6}$$

4.1 Average tube wall temperature

The average tube wall temperature at each segment can be calculated using the Newtons law of cooling as follows,

$$\dot{q} = h \, (T_{\text{w,ave}} - T_{\text{f,ave}}) \tag{4-7}$$

with $T_{\text{f,ave}}$ as the average fluid temperature. In the two-phase fluid flow, this becomes the saturation temperature of the fluid. [11]

4.2 Straight tube

Single-phase

In the single-phase region, the heat transfer coefficient h_{ph} for liquid and gas phase can be calculated from the Dittus-Boelter equation [13]

$$h_{\text{ph}} = 0.023 Re^{0.8} Pr^{0.4} \frac{\lambda}{d_{\text{i}}}$$

(4-8)

Nucleate boiling and forced convection evaporation dominated subregion

In the two-phase flow region two different flow pattern can occur which have to be separated using the Froud number Fr [14, 15].

$$Fr = \frac{G^2}{\rho_{\text{l}}^2 \, g \, d_{\text{i}}}$$

(4-9)

If Fr < 0.04, stratified flow occurs, than the Shah equation [14] is used to calculate the two-phase heat transfer coefficient h_{2ph}

$$\frac{h_{\text{2ph}}}{h_{\text{l}}} = 3.9 \cdot Fr^{0.24} \left(\frac{x}{1-x}\right)^{0.64} \left(\frac{\rho_{\text{l}}}{\rho_{\text{g}}}\right)^{0.4}$$

(4-10)

h_{l} can be determined using the Dittus-Boelter equation [13] for liquid flow only

$$h_{\text{l}} = 0.023 \left(\frac{\lambda_{\text{l}}}{d_{\text{i}}}\right) \left(\frac{G(1-x)d_{\text{i}}}{\mu_{\text{l}}}\right)^{0.8} Pr_{\text{l}}^{0.4}$$

(4-11)

If Fr > 0.04, annular flow occurs, than the Chan correlation [13, 14] is used. It states that the bubble formation h'_{b} and the convection h'_{l} are added to generate the two-phase heat transfer coefficient.

$$h_{\text{2ph}} = h'_{\text{b}} + h'_{\text{l}}$$

(4-12)

with

$$h'_{\mathrm{b}} = h_{\mathrm{b}}S \tag{4-13}$$

and

$$h'_{\mathrm{l}} = h_{\mathrm{l}}F \tag{4-14}$$

h_{b} and h_{l} are the heat transfer coefficients for the nucleate boiling and the forced convection, and S and F are correction factors.

According to Stephan [15] h_{b} for water can be determined as

$$h_{\mathrm{b}} = 3800 \left[\frac{q}{20000}\right]^{n} Fp \tag{4-15}$$

$$n = 0.9 - 0.3\, P_{\mathrm{n}}{}^{0.15} \tag{4-16}$$

$$Fp = 2.55\, P_{\mathrm{n}}{}^{0.27} \left(9 + \frac{1}{1 - P_{\mathrm{n}}{}^{2}}\right) P_{\mathrm{n}}{}^{2} \tag{4-17}$$

$$P_{\mathrm{n}} = P/P_{\mathrm{crit}} \tag{4-18}$$

with P_{crit} as the critical pressure for water (221 bar) [16].

$$S = 1/[1 + (1.15E - 6)F^{2}Re^{1.17}] \tag{4-19}$$

$$F = 1 + 2.4E4\, Bo^{1.16} + 1.37X_{\mathrm{tt}}{}^{-0,86} \tag{4-20}$$

The Martinelli parameter X_{tt} can be expressed as the following equation [16].

$$X_{\mathrm{tt}} = \left(\frac{1-x}{x}\right)^{0.9} \left(\frac{\rho_g}{\rho_{\mathrm{l}}}\right)^{0.5} \left(\frac{\mu_{\mathrm{l}}}{\mu_g}\right)^{0.1}. \tag{4-21}$$

The Reynolds number as seen in Eq. (3-17) is defined as

$$Re = G(1 - x)\, d_{\mathrm{i}}/\mu_{\mathrm{l}}. \tag{4-22}$$

Odeh, Morrison and Behnia [16] method is chosen since the geometry and operating conditions

are similar. The following table shows the comparison of straight tube geometry and operating conditions between both studies.

Table 5: Comparison of straight tube's geometry and operating conditions between the Odeh, Morrison, Behnia study and this study.

Parameters	This study	Odeh, Morrison, Behnia [16]
Inner tube diameter, d_i [mm]	10	54
System pressure [MPa]	1.0	12.0
Mass flux [kg/m² s]	7.895	349.311
Orientation	Horizontal	Horizontal

From the above table, it can be observed that the mass flux used in this study is not in the range of the ones used in Odeh, Morrison and Behnia study. However, they are using a correlation for calculating a boiling heat transfer coefficient that covers the whole range from subcooled to saturated boiling. Therefore, it can be assumed that it is applicable in this study.

A post dryout subregion [17]

The two-phase heat transfer coefficient in the post dryout region in the straight tube, h_{dry}, was calculated using the Dittus-Boelter correlation [13]. The correlation is expressed as follows,

$$h_{\mathrm{dry}} = 0.023 \left(\frac{\dot{m}\, x_{dry}\, d_i}{\varepsilon_g \mu_g} \right)^{0.8} \left(\frac{c_{p,g}\, \mu_g}{h_g} \right)^{0.4} \frac{h_g}{d_i} \qquad (4\text{-}23)$$

where $c_{p,g}$ is the heat capacity for gas and x_{dry} as the steam quality for the post dryout region. The dryout process is marked by Mori *et al.* from dryout interception x_{di}, the beginning to x_{de}, the completion. Both boundaries can be calculated according to

$$x_{\mathrm{di}} = 0.58 e^{[0.52-2.1\cdot 10^{-5} We_v{}^{0.96} Fr_v{}^{-0,02}(\rho_v/\rho_l)^{-0.08}} \qquad (4\text{-}24)$$

$$x_{\mathrm{de}} = 0.61 e^{[0.57-2.65\cdot 10^{-5} We_v{}^{0.94} Fr_v{}^{-0,02}(\rho_v/\rho_l)^{-0.08}} \qquad (4\text{-}25)$$

with We_v as the Weber number

$$We_v = \frac{G^2 D}{\rho_v \sigma} \qquad (4\text{-}26)$$

Figure 8 shows a flow pattern map by Lin [2] which can alternatively be used, to determine the steam quality at the beginning of the dryout region.
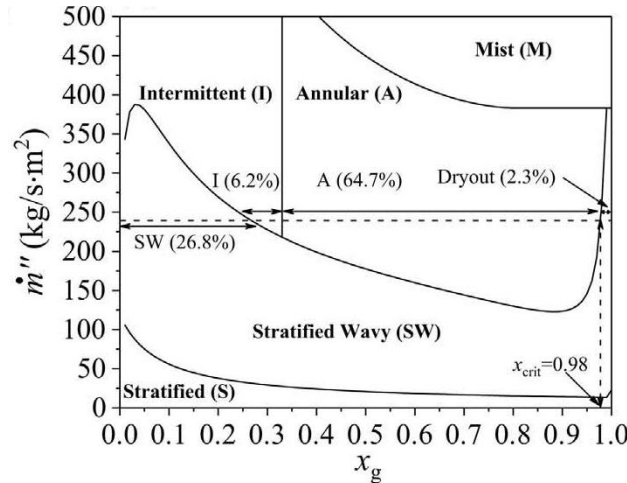
Figure 8: Flow pattern map for straight tube with din=0.005 m and q=12.3 kW/m² [2].

The average heat transfer coefficient for the two-phase flow region is defined as

$$h = \frac{L_{sc}h_{ph,l} + L_{evap}h_{2ph} + (l - L_{sc} - L_{evap})h_{ph,g}}{l} \qquad (4\text{-}27)$$

4.3 Model validation straight tube

Odeh et al. [16] experimental data for the parabolic trough solar collector was used for the validation. The comparison results between the simulation and experiment are shown in the following figure.
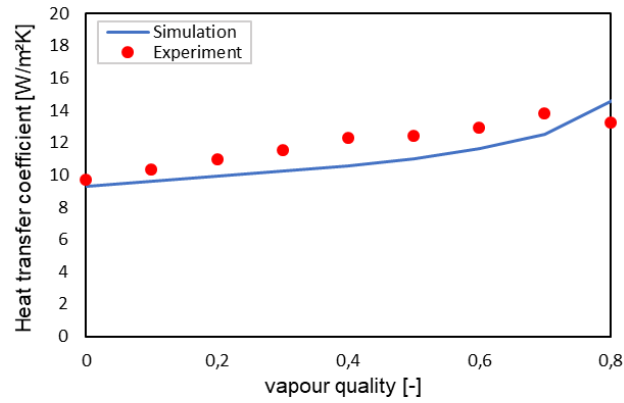
Figure 9: Heat transfer coefficient nucleate boiling and forced convection evaporation region, Odeh et al.

From the above figure, it can be observed that the simulation results agree well with the experimental results. The average and maximum deviation in Figure 9 are 10.7 % and 16.45 %, respectively.

4.4 Helical tube

Single-phase

The heat transfer coefficient in a single-phase flow can be calculated using the approach described in chapter 3. The pressure drop in the absorber tube can be calculated by using Eq. (2-13).

Nucleate boiling and forced convection evaporation dominated subregion

The two-phase heat transfer coefficient in the nucleate boiling and forced convection evaporation region in the horizontally located helical tube was calculated using the correlations proposed by Bai and Guo [17, 18]. These correlations cover the effect of both saturated nucleate boiling and forced convection, and they can be expressed as follows.

For the nucleate boiling ($1/X_{tt} < 1.2$),

$$\frac{h_{tp}}{h_{st}} = 1 + 2.21 \left(\frac{1}{X_{tt}}\right)^{0.3} \tag{4-28}$$

For the forced convection ($1/X_{tt} \geq 1.2$),

$$\frac{h_{\text{tp}}}{h_{\text{st}}} = 3.06 \left(\frac{1}{X_{\text{tt}}}\right)^{0.47} \tag{4-29}$$

here, h_{st} is the mean heat transfer coefficient inside a straight tube with base fluid (liquid water) only.

The mean heat transfer coefficient was derived based on the equation proposed by Guo et al. [17,18] and can be expressed as follows,

$$h_{\text{st}} = \frac{0.023\lambda_{\text{l}} Re_{\text{lof}}^{0.793} Pr_l^{0.4} \left(\frac{d_{\text{i}}}{D}\right)^{0.03}}{d_{\text{i}}} \tag{4-30}$$

Re_{lof} is the Reynolds number of liquid water only for nucleate boiling and forced convection. The Reynolds number of liquid water only for nucleate boiling and forced convection was derived by modifying the original one Re_{lo} and it is expressed as follows,

$$Re_{\text{lof}} = \frac{G(1-x)^{0.37} d_{\text{i}}}{\mu_{\text{l}}} \tag{4-31}$$

with G is the mass flux $(= \dot{m}/A)$. The vapor quality can be calculated from the heat balance as seen in Eq. (4-4) [21,22].

Bai and Guo's method is chosen since the helical tube's geometry and operating conditions were similar (see Table 6).

Table 6: Comparison of helical tube's geometry and operating conditions between the Bai and Guo's study and this study.

Parameters	This study	Bai und Guo's study [17]
Inner tube diameter [mm]	20	11
Helix coil diameter [mm]	250	255
Cruvataure ratio d_{i}/D [-]	0.0794	0.043
System pressure [MPa]	1.0	2.75
Heat flux [kW/m^2]	100	230-500
Mass flux [kg/m^2 s]	35.367	200-2500
Orientation	Horizontal	Horizontal

From the above table, it can be observed that the mass flux and heat flux used in our study are not in the range of the ones used in Bai and Guo's study. Hwang et al. [20] and Chung et al. [21] reported that nucleate boiling plays a significant role with respect to a heat transfer in the lower range of mass flux (G < 530 kg/m^2 s). Therefore, it can be assumed that nucleate boiling

also plays a major role in our study. Hwang et al. [20] also reported that the change of mass flux does not affect the flow boiling heat transfer in the lower range of G. Since the correlation used in Bai and Guo's study covers the effect of nucleate boiling and the mass flux used in their research is relatively low, it is considered that the correlation can also be used in our study even if the mass flux used in our research is smaller than Bai and Guo's one. Regarding the lower heat flux, it is considered that it may cause a lower heat transfer coefficient.

A post dryout subregion

The two-phase heat transfer coefficient in the post dryout region in the horizontally located helical tube was calculated using the modified Guo's correlation [19,22]. The correlation is expressed as follows.

$$h_{\text{dry}} = 0.7265 Re_{ldry}{}^{0.83} Pr_{\text{l}}{}^{0.4} \left(\frac{d_i}{D}\right)^{0.1} \left(\frac{\lambda_{\text{l}}}{d_{\text{i}}}\right) \left(\frac{1}{X_{\text{tt}}}\right)^{-0.248} \tag{4-32}$$

The above equation was derived by modifying the Guo's correlation. The Reynolds number of liquid water only for dryout Re_{ldry} was derived by modifying the Reynolds number equation for liquid only, and it can be expressed as follows,

$$Re_{ldry} = \frac{G(1-x)^{0.50} d_{\text{i}}}{\eta_{\text{l}}} \tag{4-33}$$

The transition criterion between forced convection evaporation and post dryout regimes were defined using the modified Guo's correlation [18, 23]. The correlation is expressed as follows,

$$x_{\text{dry}} = \frac{9.17 Bo^{0.288} \left(\rho_g/\rho_{\text{l}}\right)^{0.016}}{0.27 We^{0.002} De^{0.062} (D/d_{\text{i}})^{0.25}} \tag{4-34}$$

The above equation was derived by modifying the Guo's correlation. x_{dry} is the vapor quality when the dryout occurs, Bo is the Boiling number and De is the Dean number, which can be evaluated as follows [23, 24]

$$Bo = \frac{\dot{q}}{G L_{\text{evap}}} \tag{4-35}$$

$$We = \frac{G^2}{\rho_l \gamma} \tag{4-36}$$

$$De = Re_l \left(\frac{d_i}{D}\right)^{0.5} \tag{4-37}$$

$$Re_l = \frac{G d_i}{\mu_l} \tag{4-38}$$

γ is the surface tension of liquid water.

The Guo's correlation was chosen since the helical tube's geometry and operating conditions were similar. The following table shows the comparison of helical tube geometry and operating conditions between Guo's study and this study.

Table 7: Comparison of helical tube's geometry and operating conditions between Guo's study and this study.

Parameters	This study	Guo's study [19,24]
Inner tube diameter, d_i [mm]	20	15
Helix coil diameter, D [mm]	250	256
Curvature ratio (d_i/D) [-]	0.0794	0.059
System pressure [MPa]	1.0	0.5 – 3.0
Heat flux [kW/m^2]	82.715	0 - 540
Mass flux [kg/m^2 s]	35.367	0 - 2400
Orientation	Horizontal	Horizontal

The overall heat transfer coefficient for the two-phase flow in helical tubes is same as with the straight tube and is defined as Eq. (4-27).

4.5 Model validation helical tube

Heat transfer coefficient

The same geometrical data and operational conditions reported by Santini et al. [25] and Xiao et al. [26] were used in the validation. The following table shows the detailed parameters used for the model validation.

Table 8: Parameters and conditions used in Santini et al. [25] and Xiao et al. [26].

Parameters	Santini [25]	Xiao [26]
Inner diameter of the tube [m]	0.01249	0.0145
Outer diameter of the tube [m]	0.01723	0.0215
Helical coil diameter [m]	1.00	0.18
The total length of the tube [m]	32.0	8.0
System pressure [MPa]	2.0	2.0
Temperature at inlet [°C]	181.61	190.0
Averaged flux [kW/m^2]	51.0	300.0
Mass flux [kg/m^2 s]	206.0	600.0

The comparison results between the simulation and experiment are shown in the following figures.
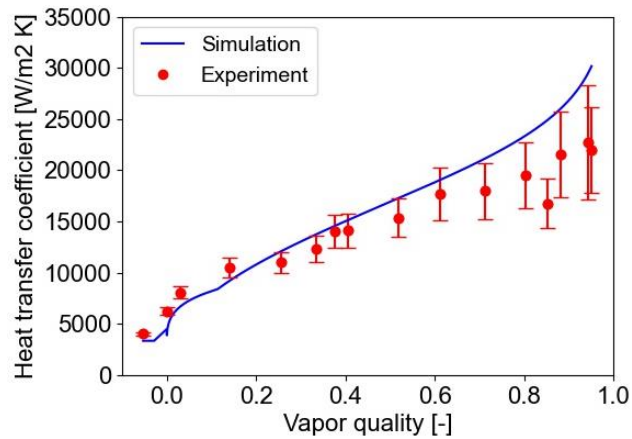
Figure 10: Heat transfer coefficient, Santini et al. [24].
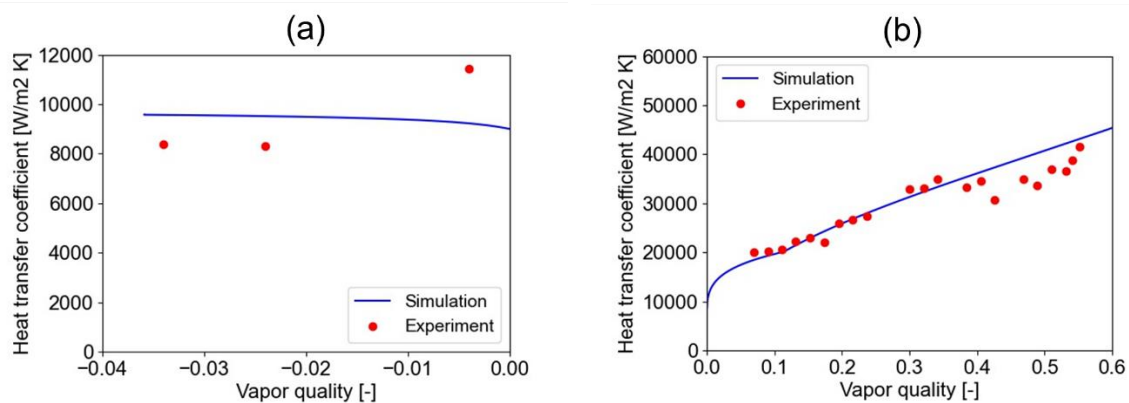
Figure 11: Heat transfer coefficient, Xiao et al. [25]; (a) subcooled inlet region; (b) nucleate boiling and forced convection evaporation region.

Here, the vapor quality is less than 0, which means the single-phase liquid flow (subcooled inlet region) occurs. From the above figures, it can be observed that the simulation results agree well with the experimental results. The average and maximum deviation in Figure 10 are 16.93 % and 39.22 %, respectively. The average and maximum deviation in Figure 11 (a) are 16.37 % and 23.81 %, respectively. The average and maximum deviation in Figure 11 (b) are 6.534 % and 17.95 %, respectively.

Fluid temperature and tube wall temperature

The simulation results were compared with the experimental results reported by Santini et al. [25] and Xiao et al. [26]. The comparison results are shown below.
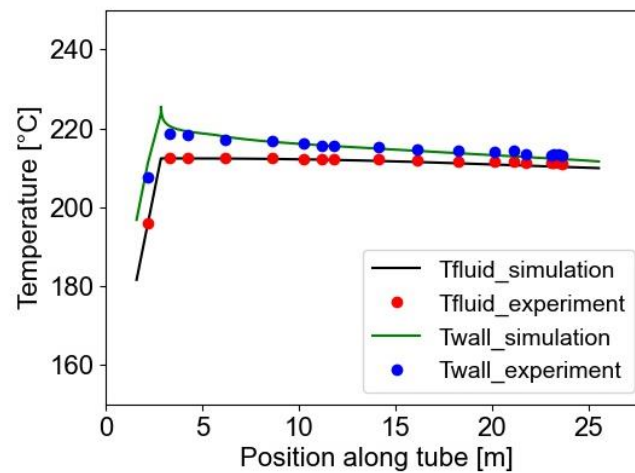
Figure 12: Fluid temperature and tube wall temperature, Santini et al. [25].
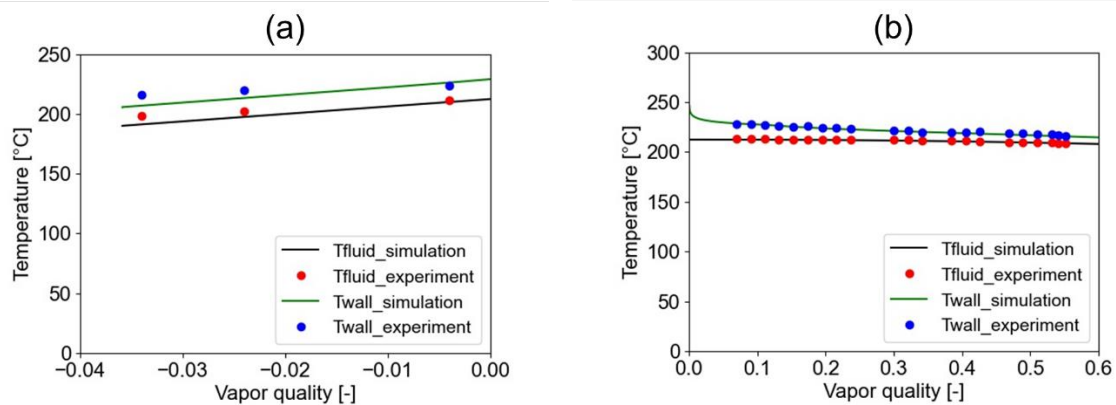
Figure 13: Fluid temperature and tube wall temperature, Xiao et al. [26]; (a) subcooled inlet region; (b) nucleate boiling and forced convection evaporation region.

From the above figures, it can be observed that the simulation results agree well with the experimental results. The average and maximum deviation of fluid temperature and tube wall temperature in Figure 12 are 0.3012 % ($T_{f,ave}$.), 0.5910 % ($T_{w,ave}$), and 0.6137 % ($T_{f,max}$), 2.212 % ($T_{w,max}$). The average and a maximum deviation of fluid temperature and tube wall temperature in Figure 13 (a) are 2.257 % ($T_{f,ave}$), 2.842 % ($T_{w,ave}$), and 3.690 % ($T_{f,max}$), 4.271 % ($T_{w,max}$). The average and maximum deviation of fluid temperature and tube wall temperature in Figure 13 (b) are 0.1932% ($T_{f,ave}$), 0.3730 % ($T_{w,ave}$), and 0.3001 % ($T_{f,max}$), 0.9658 % ($T_{w,max}$).

5 Fundamentals on System description and model development

In this chapter, the numerical method which is used in the proposed model is described. Furthermore, the numerical model and the methodology of the finite volume approach, which is used in Ansys R2020, is introduced.

5.1 Numerical Model Description

This chapter introduces the numerical model and the system design. The numerical model is based on the governing equations (continuity (2-1), momentum (2-2) and energy (2-3)) for the fluid flow inside the absorber tubes combined with the energy balance for the absorber tube and cavity wall.

$$\frac{\partial \rho}{\partial t} + \nabla(\rho \vec{v}) = S_{\mathrm{m}} \tag{5-1}$$

$$\frac{\partial}{\partial t}(\rho \vec{v}) + \nabla(\rho \vec{v} \vec{v}) = -\nabla \mathrm{p} + \nabla(\bar{\tau}) + \rho \vec{g} + \vec{F} \tag{5-2}$$

$$\frac{\partial}{\partial t}(\rho E) + \nabla(\vec{v}(\rho E + \mathrm{p})) = \nabla\left(k_{\mathrm{eff}} \nabla \mathrm{T} - \sum_{j} h_j \vec{J_j} + (\bar{\tau}_{\mathrm{eff}} \vec{v})\right) + S_{\mathrm{h}} \tag{5-3}$$

S_{m} describes the source term when mass is added to the continuous phase from the second phase, for example when phase change occurs in the condensing process.

Where p is the static pressure, $\rho \vec{g}$ the gravitational body force, $\vec{F}$ the outer body force, $\bar{\tau}$ as the stress tensor. E is the Energy, which combines the enthalpy, as well as the potential and kinetic energy. k_{eff} depends on the heat conduction and the turbulence model which is used. S_{h} includes the radiation of the model. Equation (5-1) can be used for both compressible and incompressible fluids.

The single-phase-flow model was solved applying the energy balance for the tube and cavity wall, as well as the fluid flow. The heat transfer in the cross-section area of the absorber tube is shown in Figure 14 [11]
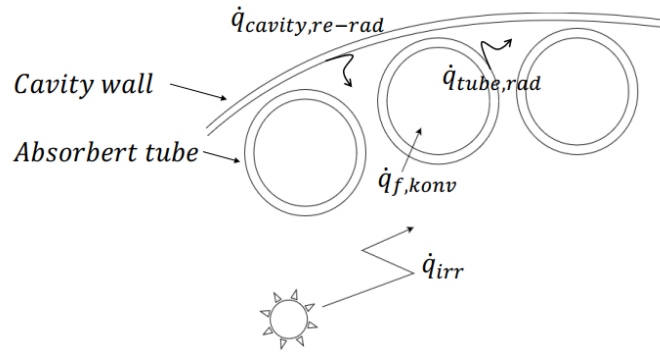
Figure 14: Heat transfer in a cross-section.

As described in chapter 2.3, the heat transfer mechanisms are the convective transport of the solar irradiation to the fluid $\dot{q}_{f,conv}$, the radiation from the heated tube outer surface area and the re-radiation from the cavity inner surface area $\dot{q}_{cavity,re-rad}$. The incoming solar irradiation $\dot{q}_{irr}$ is absorbed by the receiver tube by convective heat transfer. Because of the high absorber tube temperature, radiative heat losses to ambient occur. A part of the heat loss gets re-radiated by the cavity and backwall as re-radiative heat.

The energy balance between the heat transfer fluid and the ambient in the cavity is discretized using the Finite Volume Method. The 3D heat transfer model was solved with Ansys steady-state thermal solver version 2020 R. The model was coupled with 1D tube model of the evaporation process to generate a heat transfer coefficient for each axial tube segment. The average value for the heat transfer coefficient of the fluid is then applied to the 3D heat transfer model. The simulation provides a 1D heat flux profile to the 1D tube model azimuthal-averaging the heat flux.

5.2 Discretization

As described in chapter 5.1, the fluid flow and the energy transport can be described with partialdifferential equation which in most of the cases, can not be solved analytically. To get a numerical approximation, discreditation methods are used to linearize the differential equations and solve it as algebraic equations. The approximation applies for a small time/ volume, so for discrete point which depict the geometry of the model

The energy balance is discretized with the finite volume approach.

$$\frac{\partial}{\partial t}(\rho\phi) + \frac{\partial}{\partial x}(\rho u\phi) = \frac{\partial}{\partial x}\left(\Gamma^{\phi}\frac{\partial\phi}{\partial x}\right) + Q^{\phi} \qquad (5\text{-}4)$$

A mesh is constructed where the "finite volume" refers to a small control volume surrounding each node point of the mesh. The energy balance is spanned over the control volume which results in a set of balance equation which contains a divergence term. With the Gauss'theorem the control volume can be transferred into a surface integral. Which, according to the Ansys Fluent theory guide leads to

$$\frac{\partial}{\partial t}(\rho\phi V) + \sum_{f}^{N_{\text{faces}}}(\rho u\phi A) = \sum_{f}^{N_{\text{faces}}}\Gamma^{\phi}\nabla\phi A + Q^{\phi} \qquad (5\text{-}5)$$

By equating and applying the interpolation scheme, equation (5-5) can be transferred to algebraic form, the equation can be solved for ϕ. Using different Upwind scheme Ansys is solving the equation for the control volume center and interpolates it for the neighbor cells in the upwind direction. ϕ_{up} stand for the upwind value and is dependent on the interpolation direction. According to the upwind scheme, ϕ_{e} can be calculated according to

$$\phi_{e} = \phi_{up} if(un) > 0; \qquad (5\text{-}6)$$

respectively

$$\phi_{e} = \phi_{e} if(un) < 0; \qquad (5\text{-}7)$$

It is assumed, that the average value is valid for the whole cell. [27]

6 Modelling of tubular solar receiver for direct steam generation in Ansys

The goal is to seek an output temperature of 800 °C and a mass flow of 40 kg/h for steam and 160 kg/h for air, respectively at an efficiency rate of 70 … 80 % with a power demand of 50 kWe. The purpose of this thesis is to identify the best geometric tube configuration with the highest heat transfer rate and efficiency.

Figure 15 shows the principle of the numerical model developed.
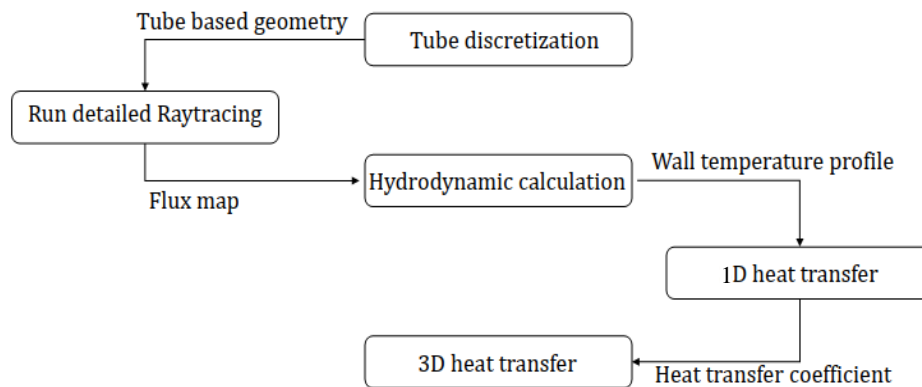
Figure 15: Modelling solar receiver.

It includes three simulation domains: raytracing, hydrodynamics and computational fluid dynamics (CFD) solved in Ansys. The raytracing simulation solves all optical aspects of the scene and is required to quantify the optical performance of the concentrated receiver. The hydrodynamic covers the boiling profile in the tube and CFD the heat losses and the transferred energy. The hydrodynamic model of the receiver tube determines the temperature profile in the absorber tube. It balances the incoming radiation, optical and thermal losses and the heat absorbed by the fluid passing through the receiver. The output is a temperature profile of the tube wall. The temperature profile of the income radiation is provided to a 3D heat transfer model in Ansys to investigate the receiver power.

6.1 Modelling Geometry

The following parameters needed to be determined.

Table 9: Geometry receiver 1 and 2.

Geometry Parameters	Process Parameters	Fixed Parameters
Cavity diameter D	Velocity v	Massflow $\dot{m}$
Tube length l		Temperature T
Tube diameter d		
Number of tubes		
Winding number		
Pitch		

6.2 Parametric study and optimization

The geometry parameters described in chapter 6.1 were investigated in different parametric studies. The receiver geometry has a high impact on how much solar radiation can actually be captured. As both receivers have a cylindrical shape, the crucial parameter is the cavity diameter and the cavity/ tube length to guarantee a good radiation of the absorber tube. To examine the influence of aperture diameter and receiver length on the collection of rays, three different receiver designs are investigated in a raytracing in SPRAY.

(a)

(b)

(c)

Figure 16: Ray Evaluation of basic model (a), increased cavity diameter and decreased tube diameter (b) and increased cavity diameter and decreased tube length (c).
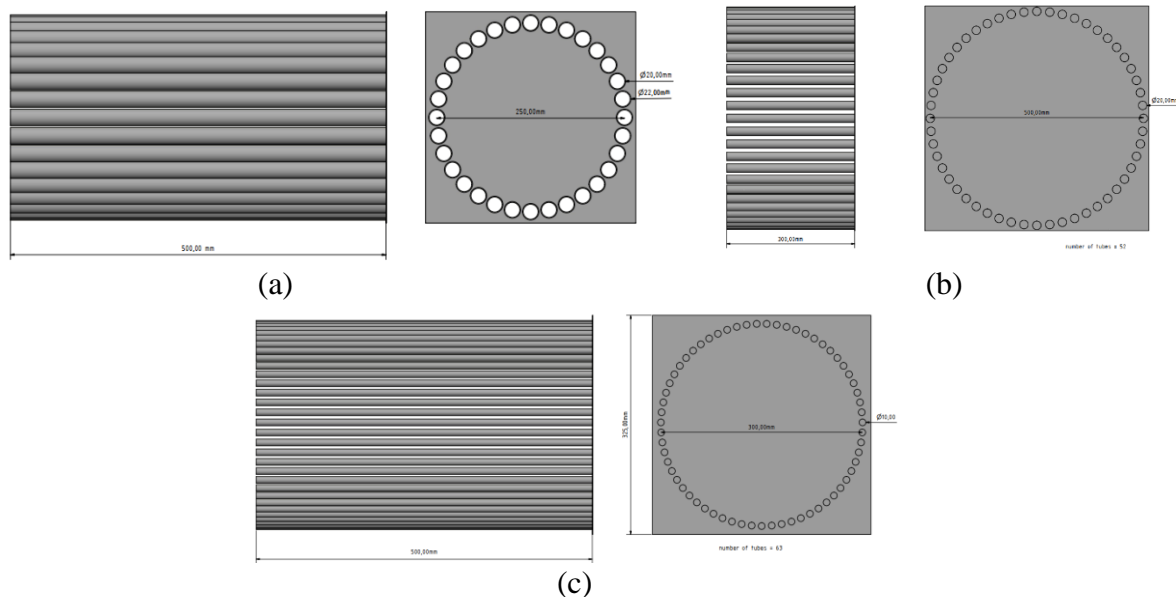
Figure 16 shows the three receiver designs, which are investigated. The basic model (Figure 16, a) has a cavity diameter of 0.2 m and a tube length of 0.5 m. The second design (Figure 16, b) has an increased diameter of 0.3 m and a tube inner diameter of 0.01m at 0.5 m tube length. The third model (Figure 16, c) has the largest cavity diameter of 0.5 m at a decreased tube length of 0.3 m. The raytracing results show, that all three models have a good ray interception. Though it must be said, that a larger cavity diameter leads to a higher ray interception rate. As a result, it can be said, that the minimum requirement for the cavity diameter is 0.2 m.

The number of tubes is investigated in a sensitivity analysis in Excel to look into the effect of the number of tubes, the velocity and the massflow on the pressure drop and the thermal efficiency. The correlation between the percentage thermal loss of the absorber at different inlet fluid flow velocities, as well as increased pressure loss was shown in the following curve.
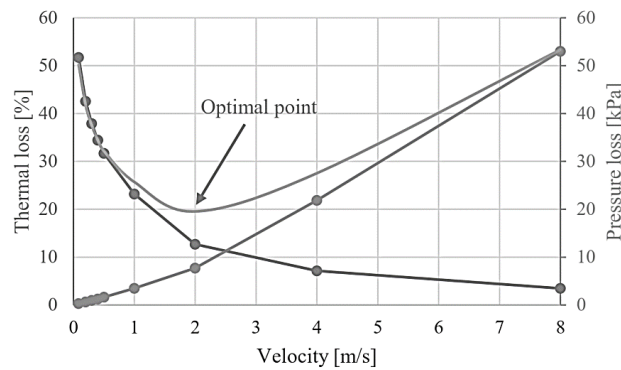
Figure 17: Optimum curve between thermal and pressure loss as function of the velocity [28].

The optimal point is at the lowest point of the curve, which in this case is at about 2 m/s (Figure 17). The curve represents the non-dimensional variables by at first dividing the pressure drop and the percentage thermal losses by their respective maximum values and second, adding these two variables. According to Slootweg [28] the optimal velocity, considering the thermal and pressure losses, is at 2m/s. This velocity was compared with the SOHTEK receiver with a similar tube design. The velocity was set to 0.4 m/s. The receiver heat transfer rate wasn't high enough, hence the tubes got damaged.

For thermal losses $\dot{Q}_{loss}$ convection $\dot{Q}_{conv}$, neglecting natural convection on the outside of the tubes and radiation $\dot{Q}_{rad}$ was considered.

$$\dot{Q}_{loss} = \dot{Q}_{conv} + \dot{Q}_{rad} \qquad (6\text{-}1)$$

The convective heat loss can be calculated according to chapter 3 for single-phase flow.

The Nusselt number was calculated with a correlation from the VDI-heat atlas [9] for the single-phase flow. The radiation heat loss was mainly suspected between the inlet aperture and the receiver's closed backside [29].

$$\dot{Q}_{rad} = \varphi_{12} \cdot A \cdot \sigma \cdot \varepsilon^2 \cdot (T_w{}^4 - T_{amb}{}^4) \tag{6-2}$$

with the Stefan-Boltzmann constant σ and the emissivity ε. φ_{12} ·is a geometric factor for the radiation between disk to parallel coaxial disk of same radius and can be calculated according to

$$\varphi_{12} = \frac{1}{2} \cdot (X - (X^2 - 4)^{\frac{1}{2}}) \tag{6-3}$$

with

$$X = \frac{2B^2 + 2}{B^2} \tag{6-4}$$

and the cavity and the backwall radius r and the distance between both surfaces b.

$$B = \frac{r}{b} \tag{6-5}$$

It is assumed that the absorber tube has a smooth surface. The pressure drop was calculated according to Eq. (2-13) and Eq. (2-14).

According to the investigation of the ray interception at the beginning of this chapter, the minimum requirement for the cavity diameter is 0.2 m. In order to form this cavity, 30 tubes are needed. This study presents a comparison of 30 and 40 tubes. At first, the correlation between velocity and heat loss is investigated. The results are shown in the following figures.
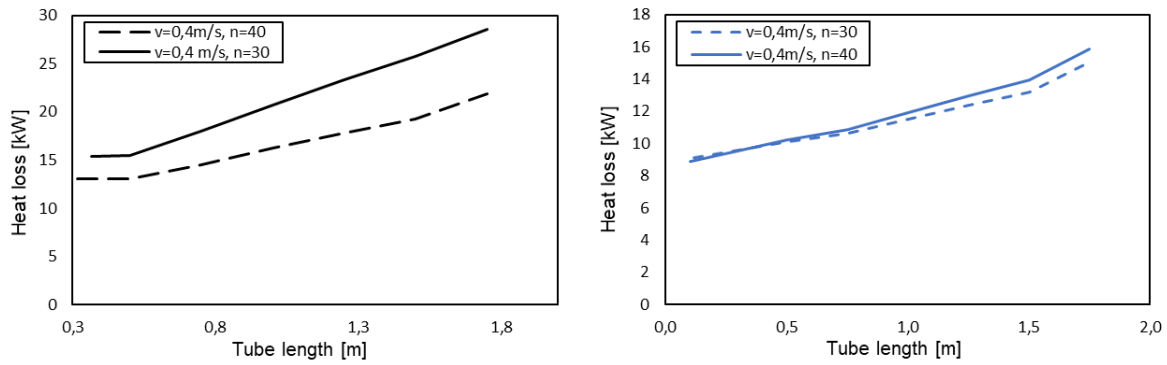
Figure 18: Heat loss at 0.4 m/s for 200 kg/h (left) and 20 kg/h (right) at different number of tubes.
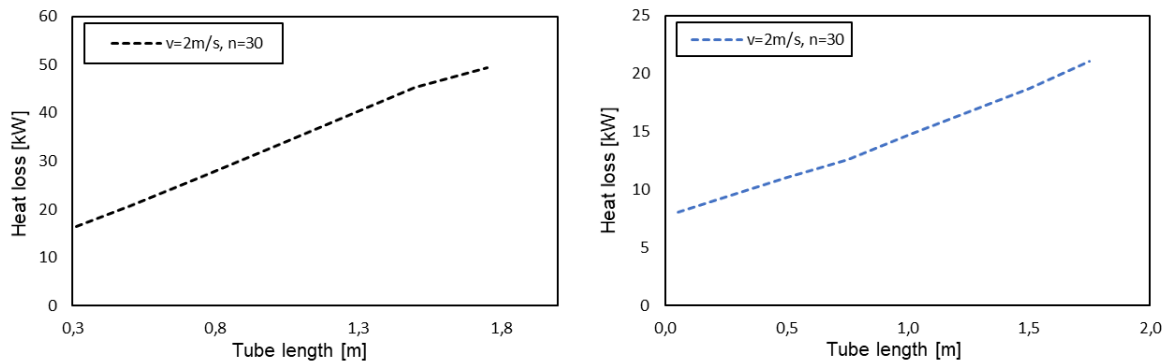
Figure 19: Heat loss at 2 m/s for 200 kg/h (left) and 20 kg/h (right) at different number of tubes.

The above figures show a linear correlation between velocity and heat losses. Furthermore, it shows that an increasing number of tubes increases the heat losses. This rise can be explained by the fact, that thereby the heat transfer area increases and thus the heat transfer rate.

At second, the pressure loss was investigated under the same conditions as the heat loss.
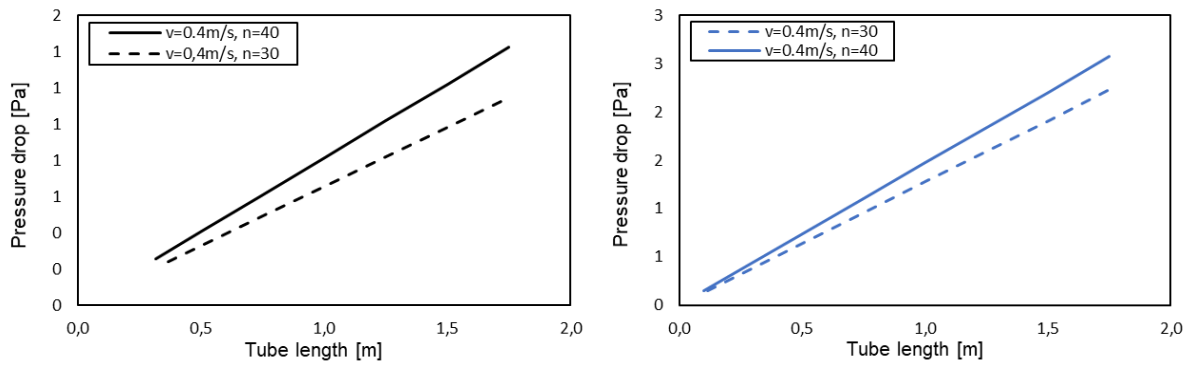
Figure 20: Pressure loss at 0.4 m/s for 200 kg/h (left) and 20 kg/h (right) at different number of tubes.
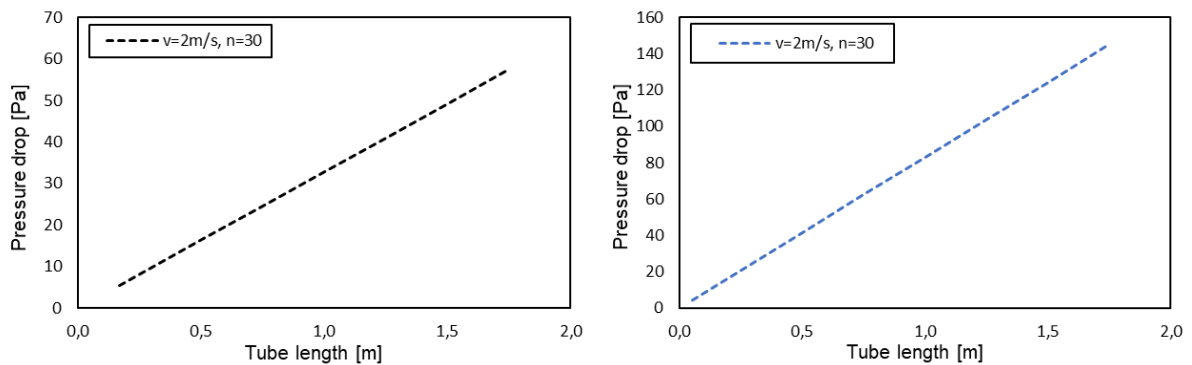
Figure 21: Pressure loss at 2 m/s for 200 kg/h (left) and 20 kg/h (right) at different number of tubes.

Figure 20 and Figure 21 show that a low pressure loss can be achieved by increasing the number of tubes and the velocity and increasing the mass flow. At last, a comparison of the optimal parameters (low velocity and low number of tubes) is presented. For that purpose the tube diameter and the mass flow rate was increased to find the optimal parameter combination.
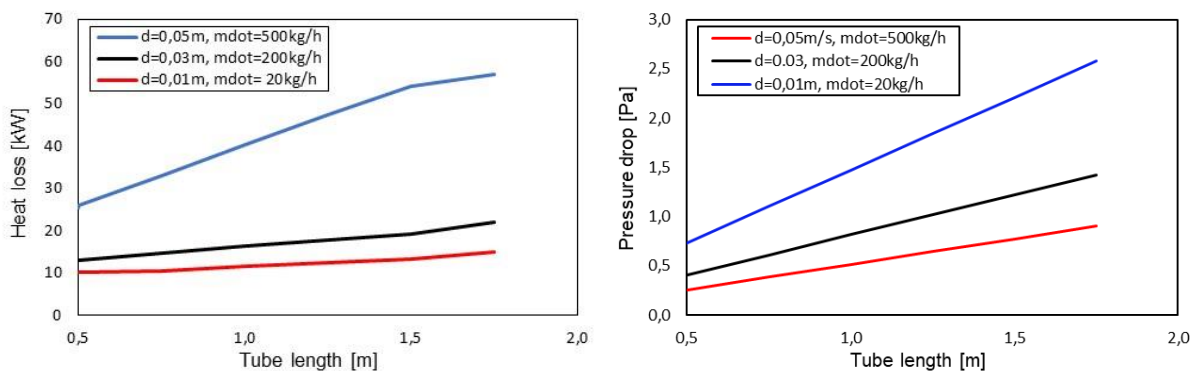
Figure 22: Heat loss (left) and pressure loss (right) for different mass flow rates.

From Figure 22 it can be seen, that a low mass flow of 20 kg/h decreases the heat loss but causes a high-pressure loss and a high mass flow of 500 kg/h causes the reverse case. For this purpose, the mass flow increased slightly to 40 kg/h for water and 160 kg/h for air.

The effect of the tube length on the heat loss was investigated in a second sensitivity study in Matlab. The fundamental for this was the integral heat balance of the system.

$$\dot{Q}_f = \dot{Q}_{irr} - \dot{Q}_{conv,evap} - \dot{Q}_{conv,superheat} - \dot{Q}_{conv,preheat} - \dot{Q}_{rad} \tag{6-6}$$

$\dot{Q}_f$ is the sum of the energy amount needed, to evaporate water, superheat steam and preheat air and is set to 100 kW, which was assumed as twice the power calculated in the process scheme, due to the doubled mass flow. The $\dot{Q}_{irr}$ is the incoming solar radiation and was set to 150 kW.
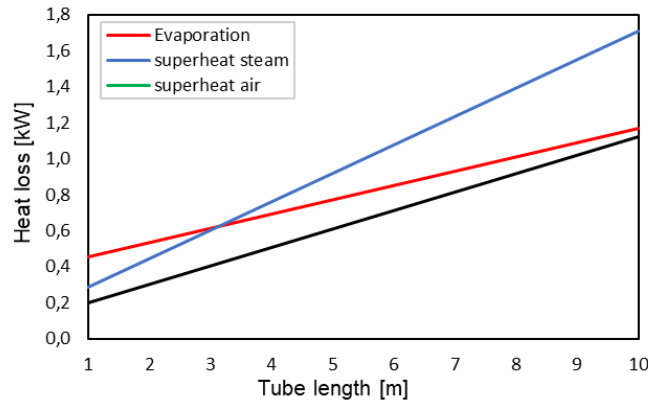
Figure 23: Heat loss for evaporation water, superheat steam, preheat air.

Figure 23 shows that the heat loss increases with increasing tube length hence to the increasing heat transfer area. As a result, the tube length should be set as short as possible.

The remaining degree of freedom, e.g. the tube length, is determined through the energy balance.

$$\dot{Q}_{irr} = \dot{Q}_{evap} \tag{6-7}$$

with

$$\dot{Q}_{evap} = \dot{m} \cdot \Delta x \cdot \Delta H_v \tag{6-8}$$

ΔH_v is the enthalpy of vaporization and Δx the difference of the flow vapor content between in- and output. The evaporation is the most complex of all three processes in the DSG receiver, because of the phase change. The critical heat flux density in the evaporation process can be determined using Figure 24.
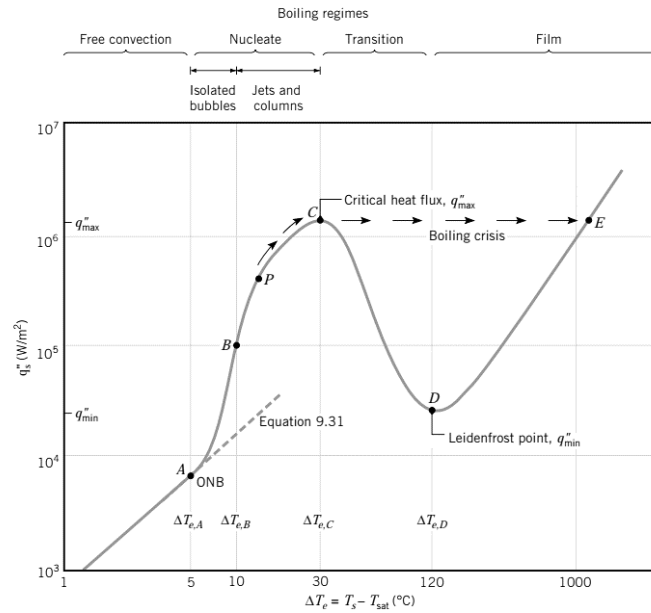
Figure 24: Boiling heat transfer curve, q heat flux as a function of the temperature difference. [30].

Figure 24 shows the heat flux q as a function of the temperature difference ΔT of the wall and the saturation temperature T_{sat}. With the energy balance of the system, the tube length can be calculated.

$$A\,\dot{q} = \dot{m} \cdot f \cdot \Delta x \cdot \Delta H_v \qquad (6\text{-}9)$$

Here f is the flow cross-section. With the heat flux from Figure 24 and Eq. (6-9) the tube length can be determined as followed.

$$l = \frac{\dot{m} \cdot \Delta x \cdot \Delta H_v}{\dot{q} \cdot \pi \cdot d} \qquad (6\text{-}10)$$

Table 10 shows the result of the calculated tube length and the needed surface are at a heat flux density of 82.715 kW/m².

Table 10: Geometry parameters receiver 1.

Process	Evaporation water	Superheat Steam	Preheat air	Sum
Mass flow [kg/h]	40	40	160	
Velocity [m/s]	0.4	0.4	0.4	
Heat transfer area [m²]	0.3725	0.1757	0.4269	
Heat flux [kW]	30.8	14.53	35.31	80.6

From Figure 22 left, it can be seen that a low massflow and inner diameter lead to a low heat loss at constant velocity. Furthermore, Figure 22 right shows a contradictory behavior. As the tube diameter and massflow increases, the pressure drop decreases. This results in a receiver length of 0.5 m and a tube diameter of 0.02 m. With the total tube surface area A_{tube} the number of tubes can be determined according to

$$A_{\text{tube}} = n \cdot \pi \cdot d \cdot l \tag{6-11}$$

Table 11 shows the set geometry parameters for each process step.

Table 11: Set parameters receiver 1.

Process	Evaporation water	Superheat Steam	Preheat air	
Tube length [m]	0.5	0.5	0.5	
Tube diameter [m]	0.02	0.02	0.02	
Number of tubes [-]	12	6	12	

To check the effectiveness of the set parameters described in table 3 a first steady-state-thermal Analysis of one tube was carried out in Ansys, applying a constant heat flux of 82715 W/m²- K. The air is used as working fluid inside the tube, and the fluid inlet temperature and mass flow rate were set to 20 °C and 3.174 g/s, respectively. The ambient temperature is set to 22 °C. The other thermophysical properties of air (e.g., thermal conductivity, density, dynamic viscosity, specific heat) refer to VDI Heat Atlas's value [9]. In this validation, the tube's radiation heat loss and natural convection loss are not considered for simplicity. The outlet air temperature became 1212.01 °C in the Ansys simulation which exceeds the heat resistant temperature of the stainless steel 1.4841 tubes of 1150 °C.

To decrease the wall temperature the incoming solar irradiation needs to be decreased, but to still obtain 800 °C outlet temperature, there are two options according to newtons first law.

Firstly, the heat transfer coefficient or second, the heat transfer area can be increased to obtain a higher heat transfer. In this case the heat transfer coefficient should be increased by adapting the velocity. At first the radiation losses should be neglected, to simplify the calculation and to take potential losses into account the target outlet temperature is increased by 8 % to have a buffer.

Table 12 shows the adapted geometry parameters of the receiver to increase the velocity and the heat transfer coefficient. According to equation (5-11) the tube number is adapted to achieve the target tube length of 0.75 m and inner diameter of 0.01 m.

Table 12: Geometry adapted for air.

Process	Evaporation water	Superheat Steam	Preheat air
Number of tubes [-]	16	8	18
Tube diameter [m]	0.01	0.01	0.01
Tube length [m]	0.75	0.75	0.75
Velocity [m/s]	0.0093	3.149	61.53
Pressure average [bar]	1	15	1
Heat transfer coefficient [W/m²K]	259.7	96.501	160.84

The simulation shows, that the increased heat transfer coefficient lead to a Fluid outlet temperature of 856.43 °C and a maximum wall temperature of 1245.6 °C. In this model the radiation was neglected, hence the expected temperature will be lower than the simulated ones.

For receiver 2, newtons law of cooling and the energy balance was used to investigate the geometry in a parametric study. The boundary condition was the wall temperature was used. At a constant heat flux of 100 kW, the temperature difference between fluid and wall should not exceed 200 K. The results show, that as the inner tube diameter increases, the wall temperature difference also decreases. In the steam superheating process, a tube inner diameter of 0.015 m was chosen, because the results are in the range of the boundary condition. Increasing the inner tube diameter would lead to a temperature difference of 294 K.

6.3 Optical modelling

For the numerical calculation of the solar receiver models, the incoming radiation is crucial to predict the heat load at the tube surface and the receiver power. Especially in the design process, it requires a validated optical model of the income radiation, that can evaluate the complex interactions between the income solar irradiation including wavelength, angle, concentration

ratio, sun shape, blocking, shading, reflectivity and the simulation of the interactions between the absorber surfaces.

Previous work at DLR on optical modelling for receiver development was for example done by Förderer [32] using the software OptiCAD. DLR also developed a raytracing tool called Spray which is especially used for the modelling of SynLight's raytracing. The solar receiver shall be operated in the high-performance simulator for concentrated solar radiation SynLight in Jülich. The radiator consists of 149 modules. To generate the flux distribution profile at first a 2D- heat flux distribution needs to be done, which will be the source for the 3D raytracing of the cavity. The 2-D flux profile of the cavity is done using DLR's simulation tool in Visual Basic for Applications (VBA). The tool models the 2D heat flux distribution on a certain area depending on the presetting of the modules. Dependent on the solar radiant power needed, a certain number of lamps needs to be turned on. The heat flux distribution can be adjusted by changing the focal point of each module.

The 2D model of the heat flux density at the cavity is done for the central test chamber and the receiver was placed at a distance x of 1 m to carry out all maintenance work. The height was set to 0 which corresponds to 1m due to the origin of the coordinate system (Figure 25).
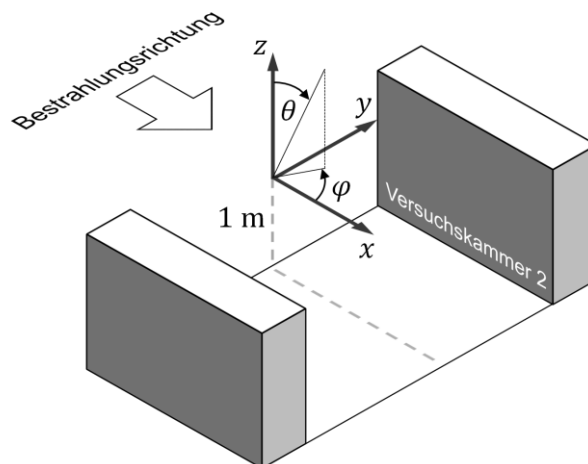
Figure 25: Origin of the coordinate system of the test chamber.

The 3D ray tracing in the cavity is carried out using the software SPRAY. It performs a wavelength resolved ray tracing simulation using the following input variables.

- Light source that emits rays
- Objects like mirrors, light scatters, absorbers or interfaces that change the direction of rays or absorb them

- Screen, detectors and detector arrays to gather information about the distribution of radiation in the setup

For a quantitative analysis the ray tracing software simulates the light source emitting rays in a certain direction. The software pictures the rays getting re-directed and absorbed in the cavity by the tubes and the backwall. The outcome of the ray tracing is mapped as a non-uniform heat flux distribution in the 3D cavity receiver. [32] The load profiles can be applied as a boundary condition, as user defined function in the CFD model. Figure 26 show the simulated heat flux distribution implemented to Ansys for receiver 2. To avoid high temperatures at the cavity's backwall and implicitly efficiency losses, the heat flux was distributed on the outline of the cavity.

(a)   (b)
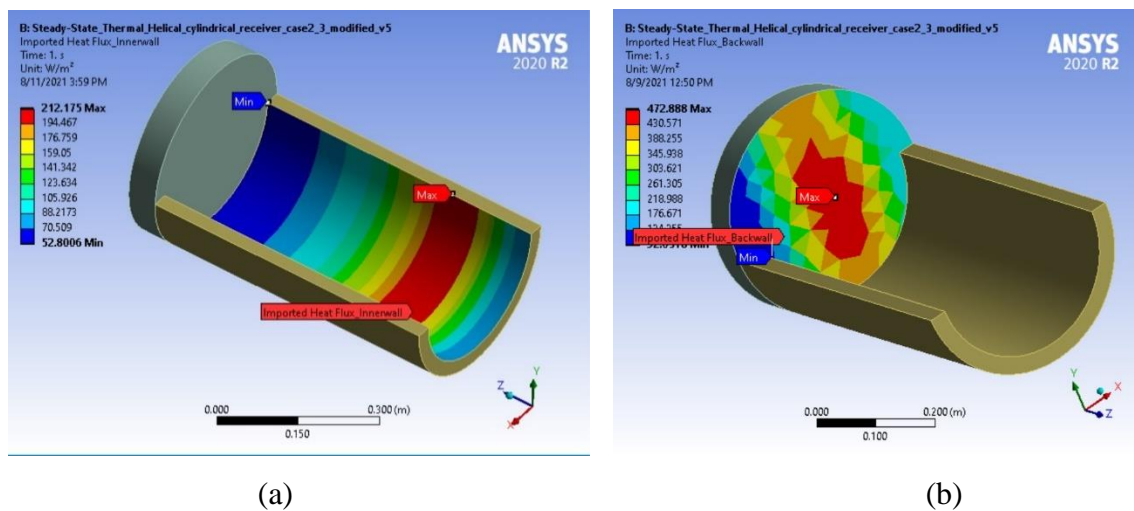
Figure 26: Imported Raytracing data cavity wall (a) and backwall (b).

7   Numerical modelling in Ansys

A thermal 3D heat transfer model is coupled to a 1D fluid flow model based on the CAD model of the receiver is used to analyze the thermal behavior. To simulate fluid flow applications in Ansys, Fluent is mostly used. It can be used for a wide range of applications and can be adapted to each case quickly. Though the computational time of Ansys Fluent and the error tracking is comparable hard. For this reason, the fluid flow simulation was carried out using the steady-state thermal analysis in Ansys version 2020 R2, which has a much lower computational time and implicitly cost then Fluent. The Ansys model uses the local heat transfer to fluid by a one-dimensional fluid element, the heat flux distribution, radiative heat exchange and forced convection to ambient. The convection of fluid flow is considered at the tube inner wall area. The natural convection is considered from the outer and inner cavity wall. The conduction loss is investigated from the cavity wall. The radiative heat exchange occurs among the backwall, the cavity inner surface area and the absorber tubes outer surface area.

7.1   Geometry

The geometry is constructed in Autodesk Inventor and imported to Ansys Workbench as *step file. Figure 27 and Figure 28 show the CAD model. The geometry is extended by lines to be used later on as 1D fluid flow elements. Further, the geometry is sliced for better meshing and definition of boundaries.

Figure 27: Extended CAD model – receiver 1.
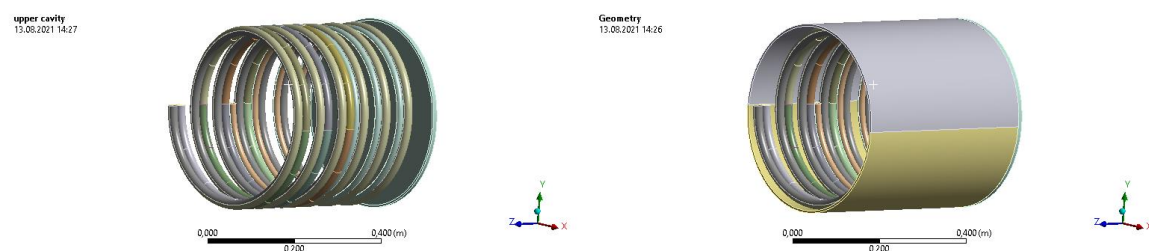
Figure 28: Extended CAD model – receiver 2.

Table 13 and Table 14 show the geometry parameters of both receivers. The absorber tube is made from high temperature stainless steel grade 1.4841, 1 mm thickness, similar to the Future Fuels receiver [6]. The spiral tube was insulated with a housing ("PROMAFORM 1600") to prevent heat losses and to hold the cavity in place.
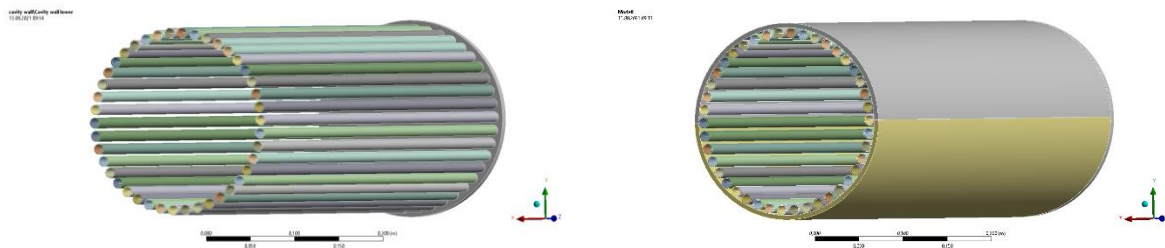
Table 13: Geometry parameters receiver 1.

Process	Evaporation water	Superheat Steam	Preheat air
Cavity inner diameter [m]	0.2	0.2	0.2
Tube length [m]	0.75	0.75	0.75
Number of tubes [-]	16	8	18
Tube inner diameter [m]	0.01	0.01	0.01
Tube outer diameter [m]	0.012	0.012	0.012
Tube length [m]	0.75	0.75	0.75

Table 14: Geometry parameters receiver 2.

Process	Evaporation water	Superheat Steam	Preheat air
Cavity inner diameter [m]	0.425	0.425	0.425
Cavity length [m]	0.45	0.45	0.45
Number of tubes [-]	1	1	1
Winding number [-]	3.25	3.0	6.0
Pitch [m]	0.067	0.067	0.067
Tube inner diameter [m]	0.02	0.015	0.02
Tube outer diameter [m]	0.022	0.017	0.022
Tube length [m]	4.090	3.709	7.551

7.2 Mesh

The geometry is meshed with solid elements, the fluid with one-dimensional fluid element allowing heat and mass transport. The surface elements are used to model the boundaries like absorbed radiation, radiative heat exchange, and forced convection (inside and outside). Both receivers achieve an excellent mesh with a skewness of 0.12 for receiver 1 and 0.07 for receiver 2, respectively. The skewness is an important value to assess the mesh structure's quality. The skewness indicates how close mesh cell to the ideal cell shape is.

Figure 29: FE mesh - helical cylindrical receiver (the upper cavity wall is omitted).

7.3 Thermal boundaries

7.3.1 Heat and mass transfer

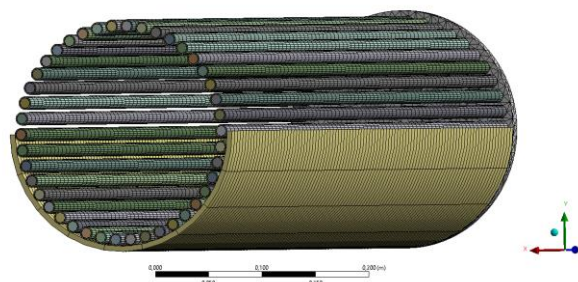The heat transfer to the working fluid is represented by a one-dimensional fluid element that can transfer heat and mass. The heat transfer coefficient was calculated using the approach described in chapter 3 for single-phase flow and chapter 4 for two-phase flow, respectively.

The heat transfer is applied as a 1D fluid element on the inside of the absorber tubes, which means there is no temperature profile in the cross section area of the fluid. The fluid element calculates the bulk fluid temperature depending on the local heat transfer from the inner tube wall, the mass flow, and the fluid properties. The heat transfer coefficient for natural convection from the inner cavity wall was calculated using Eq. (2-8). For the natural convection from the outer cavity wall according to Lin et al. [2] a constant value of 5 W/m²K was assumed. The following tables show the fluid flow values for both receiver.

Table 15: Fluid flow values – receiver 1.

Process	Evaporation water	Superheat Steam	Preheat air
Mass flow per tube [kg/s]	0.000694	0.00139	0.001543
Inlet temperature [°C]	20	600	70
Heat transfer coefficient [W/m²K]	1201.786	155.283	96.37
Pressure [bar]	1	10	1
Heat flux [kW/m²]	100	100	100

Table 16: Fluid flow values – receiver 2.

Process	Evaporation water	Superheat Steam	Preheat air
Mass flow per tube [kg/s]	0.0111	0.0111	0.0444
Inlet temperature [°C]	20	180	20
Heat transfer coefficient [W/m²K]	347.27-10172.49	580.59	630.07
Pressure [bar]	10	10	10
Heat flux [kW/m²]	100	100	100

The inlet temperature for receiver 1 for superheating steam is set to 600 °C. The first simulations at different fluid flow values showed, that receiver 1 could not reach the target outlet temperature of 800 °. Consequently, the inlet temperature for receiver 1 were adapted. The steam accumulator increases the temperature of the evaporated water and can increase the stram inlet temperature to 600 °C. The air can supplied at an inlet temperature of 70 °C, because of the heating caused by the hydraulics and other components of the receiver. The inlet of the

superheated steam for receiver 2 was set to 180 °C which is the evaporation temperature at 10 bars.

7.3.2   Radiative heat exchange

The model considers the infrared grey diffuse heat exchange between the absorber tubes and the inner and outer cavity wall. The tube surfaces and cavity inner surfaces were modeled with an emissivity of 0.9 and 0.5, respectively. Since the model is an open cavity, the infrared grey diffuse heat exchange also occurs between the absorber tubes and the ambient, and the inner cavity wall and the ambient. For the outer cavity wall the emissivity was set to 0.8. [2] The ambient temperature was set to 22 °C.

7.4   Validation Ansys simulation

The Ansys simulation is validated in two ways; Constant wall temperature and Constant heat flux. The model used in this validation is shown in Figure 30.
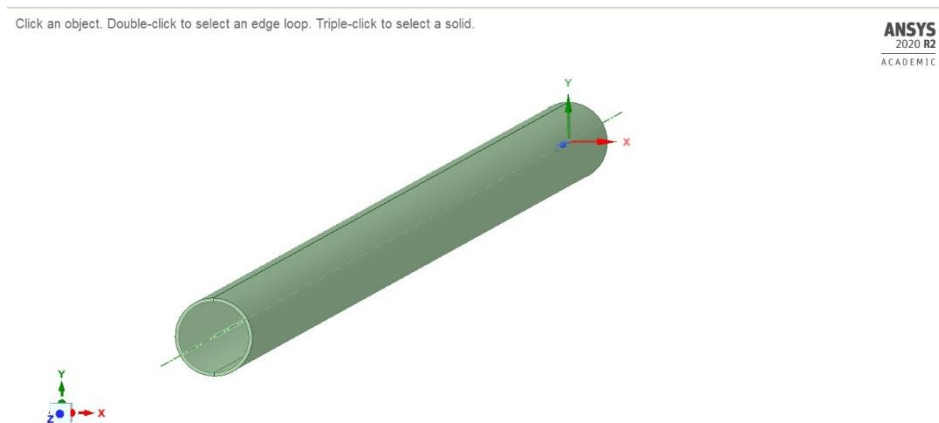
Figure 30: Simple tube model.

The simple tube model is used to simplify the calculation process. The inner and outer diameter and length were set to 0.02 m, 0.022 m, and 0.5 m, respectively. The material of the tube is set to aluminum.

7.4.1   Constant wall temperature

The constant wall temperature will be used for simulating the water evaporation. The outlet fluid temperatures calculated by the mathematical model shown below and simulated by Ansys

were compared to confirm the validity. The air was used as working fluid inside the tube, and the fluid inlet temperature and mass flow rate is set to 20 °C and 3. 174 g/s, respectively. The ambient temperature and tube wall temperature is set to 22 °C and 1000 °C. The other thermophysical properties of air (e.g., thermal conductivity, density, dynamic viscosity, specific heat) refer to VDI Heat Atlas's value [9].

Mathematical equations

The thermal energy absorbed by the flowing fluid can be expressed with

$$Q_f = \dot{m}_f \, c_{p,f} \, (T_{out} - T_{in}) \qquad (7\text{-}1)$$

The above equation can also be expressed as follows by using the heat transfer coefficient for forced convection.

Substituting Equations (7-1) and (7-2) into Eq. (7-2),

$$h_f \, A_{tube} \frac{(T_{out} - T_{in})}{ln\left(\frac{T_w - T_{in}}{T_w - T_{out}}\right)} = \dot{m}_f \, c_{p,f} \, (T_{out} - T_{in}) \qquad (7\text{-}3)$$

Rearranging the above equation,

$$T_{out} = T_w - (T_w - T_{in}) \, e^{-\frac{h_f \, A_{tube}}{\dot{m}_f \, c_{p,f}}} \qquad (7\text{-}4)$$

The outlet fluid temperature can be calculated by using the above equation. [9] The heat transfer coefficient for forced convection can be calculated by using the equations for straight tubes described in chapter 3.

Results

In the Ansys simulation, a steady-state thermal model is used to investigate the temperature of the air flowing inside the simple tube. In the simulation, the radiation heat loss or the natural convection loss from the tube outer surface area is not considered since the tube wall

temperature will be kept constant at 1000 °C. In other words, those heat losses don't affect the fluid temperature in the simulation at the constant wall temperature.

The outlet air temperature became 410.24 °C in the Ansys simulation. The comparison results between the calculation using the mathematical model shown above and the Ansys simulation are shown in Table 17.

Table 17: Comparison results.

Parameter	Mathematical model	Ansys simulation
Outlet air temperature	413.77 °C	410.24 °C

From Table 17, it is obvious that there is a good agreement between the mathematical model's result and the Ansys simulation result. Therefore, it can be concluded that the Ansys simulation is validated in a constant wall temperature condition.

7.4.2 Constant heat flux

The constant heat flux will be used later for simulating superheated steam and air. The air is used as working fluid inside the tube, and the fluid inlet temperature and mass flow rate are set to 20 °C and 0.003174 kg/s, respectively. The heat flux to the tube and the ambient temperature are set to 82715 W/m^2 and 22 °C. The other thermophysical properties of air (e.g., thermal conductivity, density, dynamic viscosity, specific heat) refer to VDI Heat Atlas's value [8]. In this validation, the tube's radiation heat loss and natural convection loss are not considered for simplicity.

Mathematical equations

Since the heat losses from the tube are not considered, all of the heat flux provided to the tube will be absorbed by the flowing fluid.

Rearranging Eq. (7-1),

$$T_{\text{out}} = T_{\text{in}} + \frac{\dot{q}\, A_{\text{tube}}}{\dot{m}_f\, c_{p,f}} \tag{7-5}$$

The outlet fluid temperature can be calculated by using the above equation. The inlet and outlet wall temperature $T_{w,\text{in}}$ and $T_{w,\text{out}}$ can be calculated by using Newton's law of cooling as shown below.

$$\dot{q} = h_{f,\text{in}}\left(T_{w,\text{in}} - T_{f,\text{in}}\right) = h_{F,\text{out}}\left(T_{w,\text{out}} - T_{f,\text{out}}\right) \tag{7-6}$$

Both $h_{F,\text{in}}$ and $h_{F,\text{out}}$ can be calculated using Eq. (2-9). [9]

Results

In the Ansys simulation, a steady-state thermal model is used to investigate the temperature of the air flowing inside the simple tube. The outlet air temperature results in 912,01°C in the Ansys simulation. The comparison between the mathematical model shown in Section 2.1 and the Ansys simulation is shown in Table 18.

Table 18: Comparison results.

Parameter	Mathematical model	Ansys simulation
Outlet air temperature [°C]	700.7	695.2
Inlet wall temperature [°C]	1590.6	1656.782
Outlet wall temperature [°C]	2368.8	2368.8

From Table 18, it is obvious that there is a good agreement between the mathematical model and the simulation results. Moreover, the outlet fluid and the inlet wall temperature have a good agreement. However, the outlet wall temperature has a bigger difference when compared to other parameters. Since the mathematical model calculation is conducted in the average fluid temperature, it can be considered that this is one reason why the difference occurred. Although this difference should be considered carefully, the difference is not significant (less than 5.5 %), so it can be concluded that the Ansys simulation is validated at a constant heat flux. The validated model is used for simulating the receiver. In the next chapter the coupling of both models is explained.

7.5 Model coupling

The validated Ansys model can then be used for the receiver investigation. The geometry is therefore replaced by the geometry of receiver 1 and 2. The following figure shows how both models are coupled.
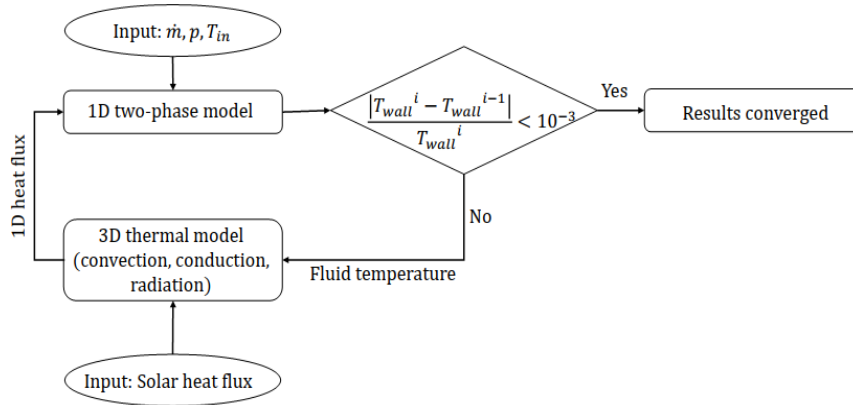

Figure 31: Schematic of the coupling between the 1D tube model and the 3D heat transfer model.

At first, the heat transfer coefficient and the tube inner wall surface were calculated using the massflow, pressure and inlet temperature as input parameters according to chapter 3 for the single-phase flow and chapter 4 for the two-phase flow, respectively. For the evaporation process the absorber tube was split into multiple segments. The 3D thermal model uses the average heat transfer coefficient of the fluid and the inner wall temperature which were calculated using the 1D two-phase flow fluid model to determine the local heat flux distribution applied. The 1D model was used to calculate the local heat transfer coefficient as well as the temperature for each segment with the heat flux obtained from the numerical model. This iteration was repeated until the wall temperature fulfills the convergence criteria. The convergence criterion was set to 10^{-3}. According to Lin [2], this value leads to an energy balance deviation smaller than 0.5 %.

$$\frac{\left|T_{\mathrm{w}}^{i} - T_{\mathrm{w}}^{i-1}\right|}{T_{\mathrm{w}}^{i}} < 10^{-3} \qquad (7\text{-}7)$$

Here the exponents i and i-1 are the iterations of each node. For analyzing superheating steam and air, the outlet fluid temperature, thermal losses and thermal efficiency were determined using the 3D thermal model. The outlet fluid temperature for superheated air and steam were analyzed by only considering Ansys. The model coupling is used to investigate the phase change in the evaporation process.

The iteration for receiver 1 converges after 7 iterations and a total computational time of 10 h and 51 mins and 6 iterations and 7 h for receiver 2.

8 Results and discussion

8.1 Steady state thermal analysis

The inlet of the fluid was set to the front. This leads to higher temperatures and radiation at the back of the cavity but due to the cavity walls the radiation can be re-radiated and absorbed again by the absorber tubes. The following figures show the results of the thermal model (temperatures).

(a) (b)

Figure 32: Ansys simulation results receiver 1; (a) entire temperature without radiation; (b) with radiation.

(a) (b)

Figure 33: Ansys simulation results receiver 2; (a) entire temperature without radiation; (b) with radiation.

(a)   (b)
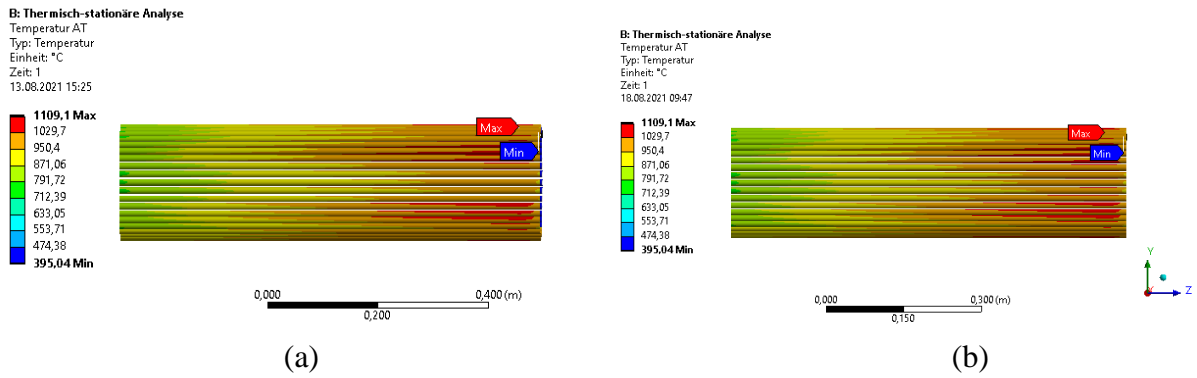
Figure 34: Ansys simulation results receiver 1; (a) absorber tube temperature without radiation; (b) with radiation.

(a)   (b)
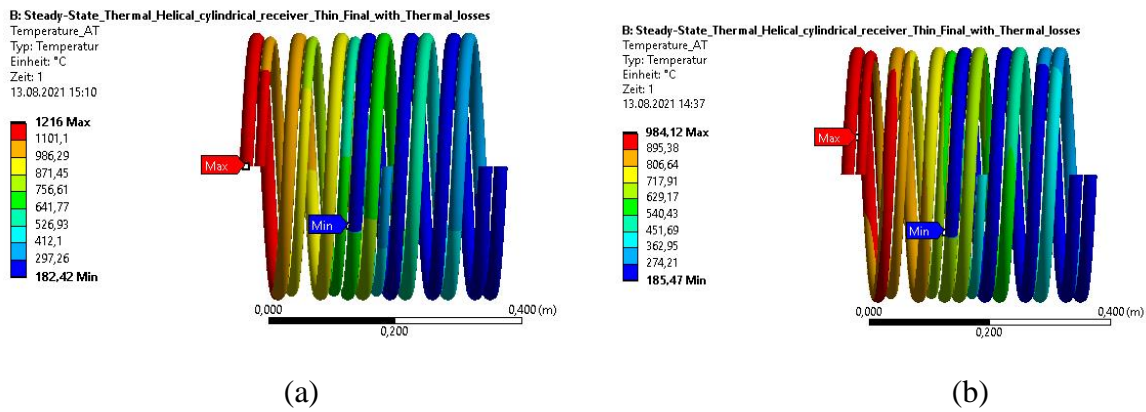
Figure 35: Ansys simulation results receiver 2; (a) absorber tube temperature without radiation; (b) with radiation.

(a)   (b)

Figure 36: Ansys simulation results receiver 1; (a) temperature superheating air without radiation; (b) with radiation.

(a)   (b)

Figure 37: Ansys simulation results receiver 2; (a) temperature superheating air without radiation; (b) with radiation.

(a)   (b)

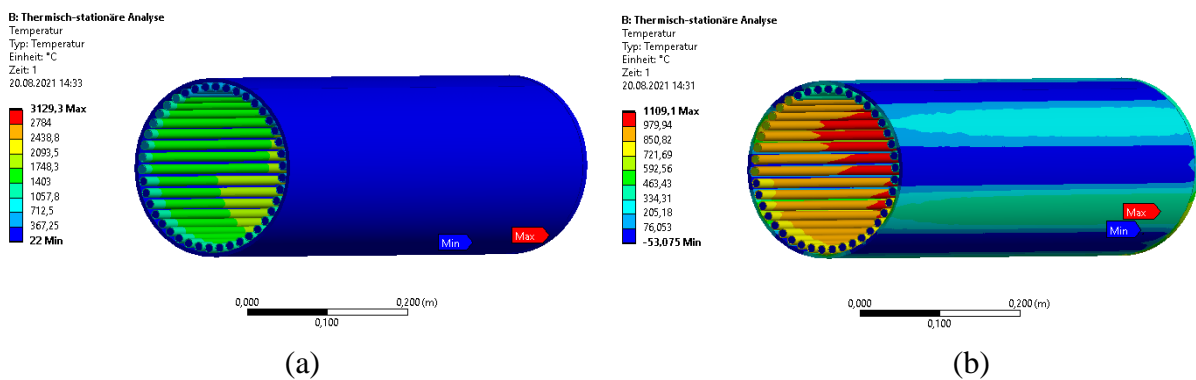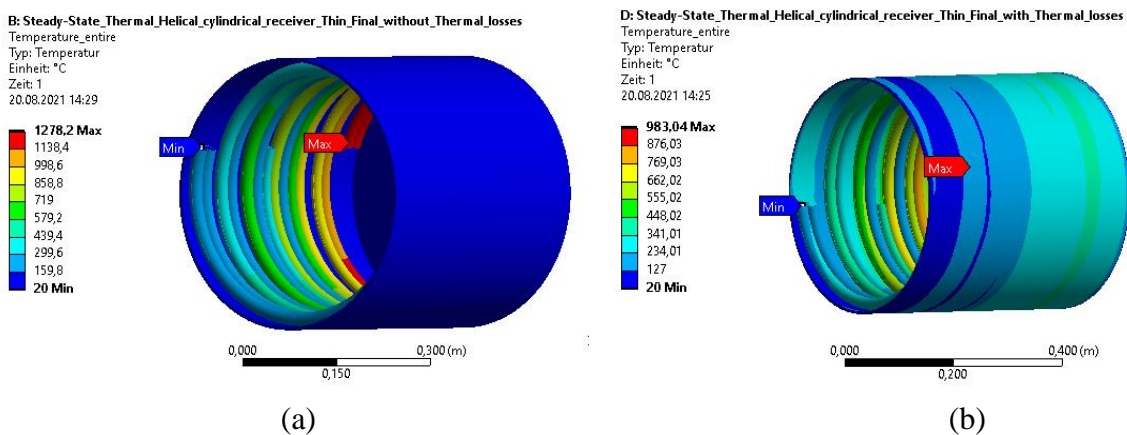**Figure 38:** Ansys simulation results receiver 1; (a) temperature superheating steam without radiation; (b) with radiation.

(a)   (b)

Figure 39: Ansys simulation results receiver 2; (a) temperature superheating steam without radiation; (b) with radiation.

The comparison results of the Ansys simulations are shown in Table 19 and Table 20.

Table 19: Comparison of absorber tube temperature with radiation for receivers 1-2.

Parameter	Receiver 1	Receiver 2	Heat resistance stainless steel 314 [33]
Temperature	1109.1 °C	984.12 °C	1150 °C

Table 19 shows the absorber tube outer surface temperature and the heat resistance temperature of the absorber tube temperature. It evaluates that both receiver temperatures don't exceed the heat resistance temperature of the tube material.

Table 20: Comparison of superheating steam and air temperature for receivers 1-2.

Parameter	Superheating air		Superheating steam	
	No radiation	Radiation	No radiation	Radiation
Receiver 1	1907.8 °C	799.8 °C	1478.9 °C	892.15 °C
Receiver 2	861.66 °C	848.25 °C	879.68 °C	876.6 °C

From Table 20, it is obvious that the fluid temperature decreases when radiation is considered in receivers 1 and 2 because of the high thermal losses. From the results, it can be seen that both proposed receivers can fulfil the target temperatures, though receiver 1can just reach the target temperature for superheating air at a reduced mass flow of 100 kg/h.

8.2 Water evaporation

The two-phase heat transfer coefficient as well as the tube inner wall temperature was calculated according to chapter 4 and applied to the 3D model as described in chapter 7.5. The following figures show the results of the thermal model (temperatures).

(a)   (b)
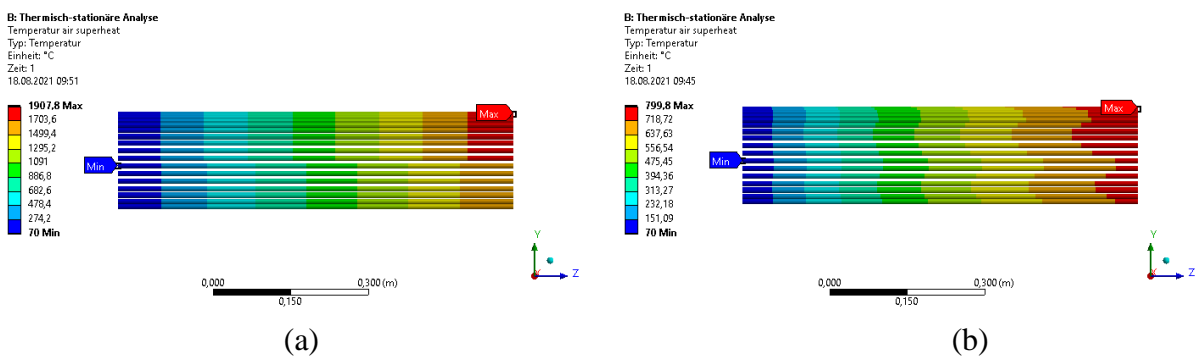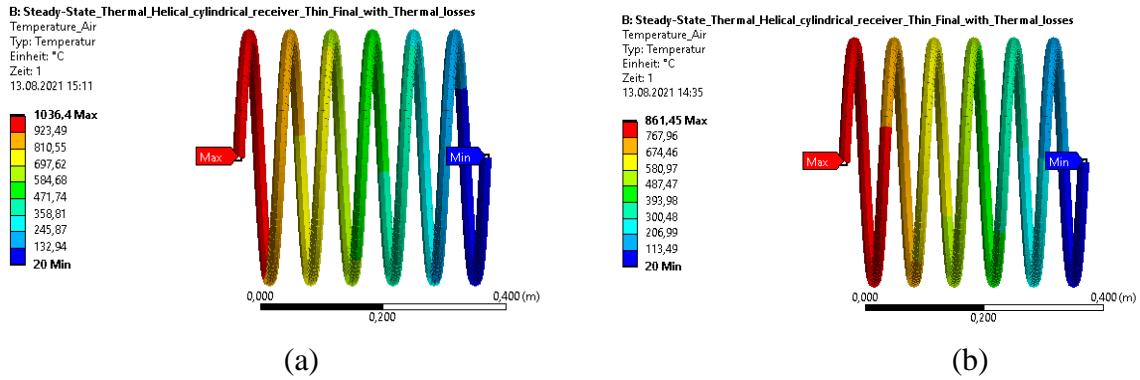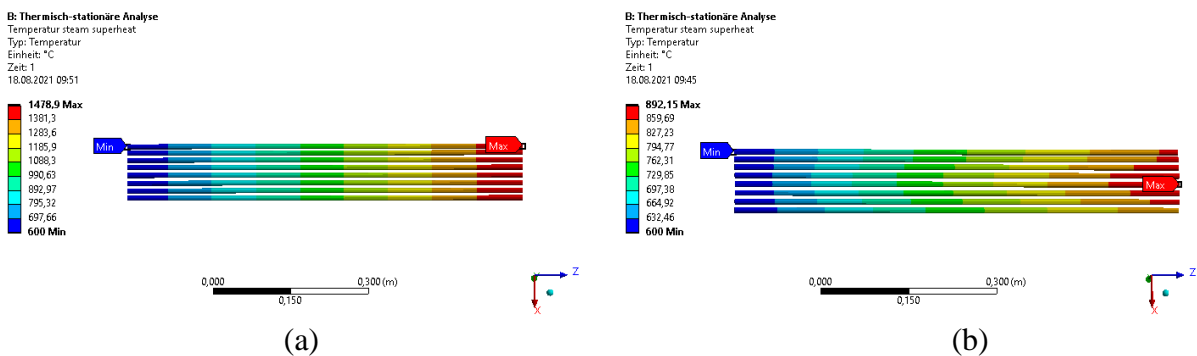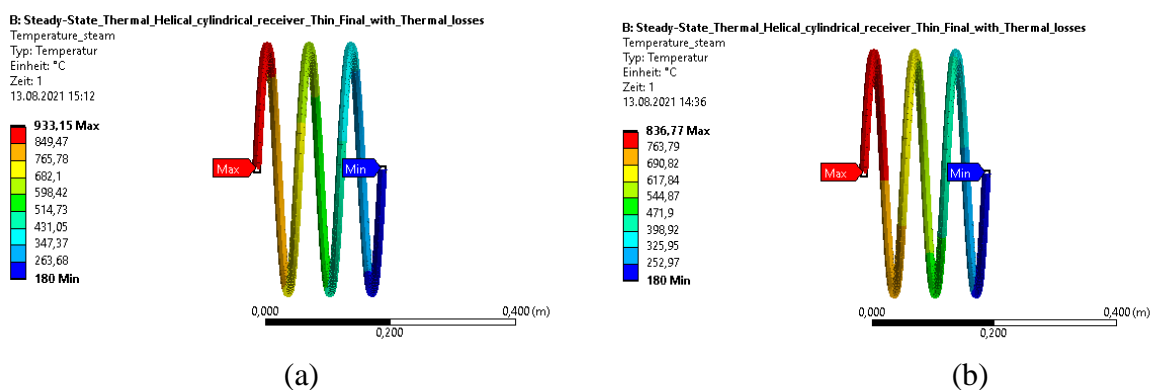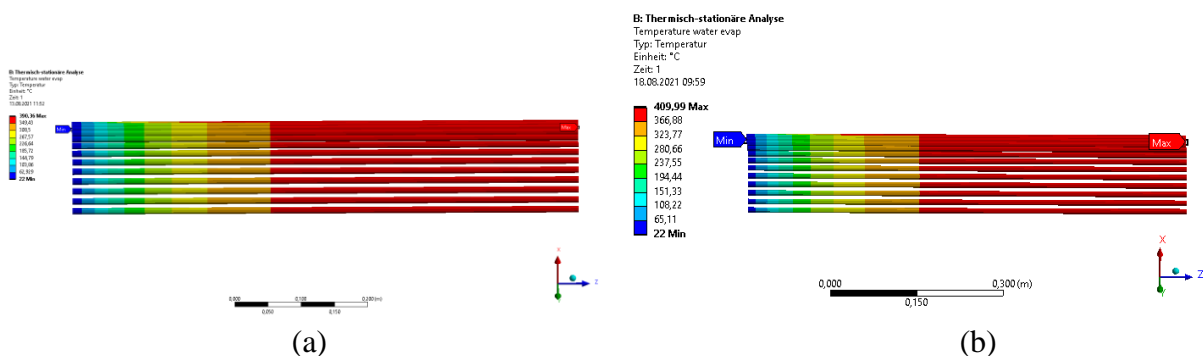
Figure 40: Ansys simulation results receiver 1; (a) temperature evaporation without radiation; (b) with radiation.

<div align="center">(a)   (b)</div>
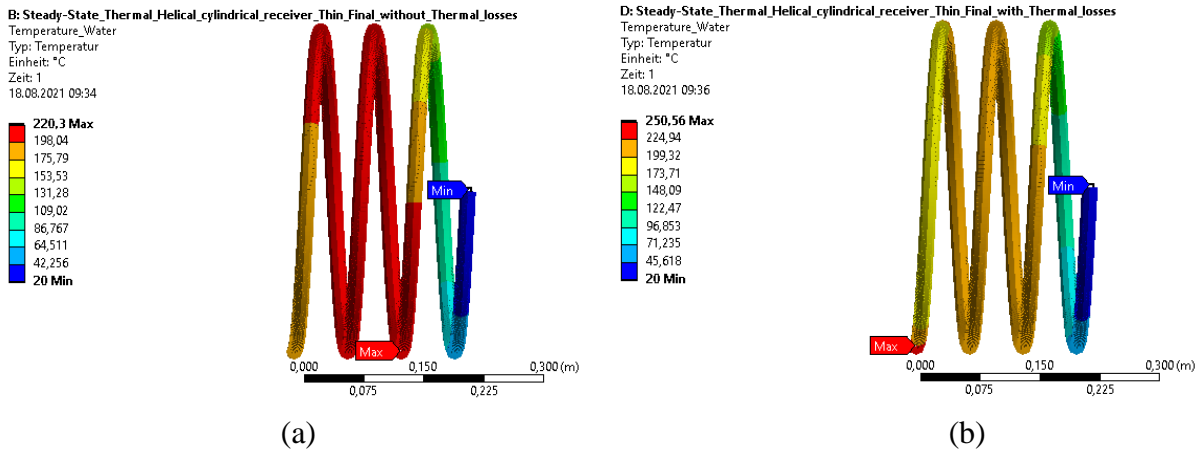
Figure 41: Ansys simulation results receiver 2; (a) temperature evaporation without radiation; (b) with radiation.

The comparison results of the Ansys simulations are shown in Table 21.

Table 21: Comparison of superheating steam and air temperature for receivers 1 and 2.

Parameter	Evaporation	
	No radiation	Radiation
Receiver 1	390.36 °C	409.99 °C
Receiver 2	220.3 °C	250.56 °C

From Table 21, it can be seen that the outlet fluid temperature is higher when radiation is considered. Because the evaporation fluid has the lowest temperature, compared to air and steam, it absorbs a huge amount of energy from the other absorber tube and cavity wall since it has a high emissivity (0.9). Furthermore, the results show, that both receivers can fully evaporate water up to temperatures of 409.99 °C (receiver 1) and 250.56 °C (receiver 2).

8.3 Thermal efficiency

The thermal efficiency was calculated according to Eq. (2-12). The comparison results are shown in in the following tables.

Table 22: Comparison of the thermal efficiency for receivers 1 and 2 for superheating air with radiation.

	Tube surface area	Heat flux	Receiver power	Thermal Efficiency
Receiver 1	0.5094 m²	50.847 kW	22.391 kW	0.429
Receiver 2	0.5219 m²	21.219 kW	41.282 kW	0.791

Table 23: Comparison of the thermal efficiency for receivers 1 and 2 for superheating steam with radiation.

	Tube surface area	Heat flux	Receiver power	Thermal Efficiency
Receiver 1	0.226 m²	22.619 kW	7.127 kW	0.315
Receiver 2	0.194 m²	19.809 kW	16.368 kW	0.826

Table 24: Comparison of the thermal efficiency for receivers 1 and 2 for evaporation with radiation.

	Tube surface area	Heat flux	Receiver power	Thermal Efficiency
Receiver 1	0.452 m²	135.717 kW	60.464 kW	1.337
Receiver 2	0.2827 m²	28.268 kW	32.028 kW	1.133

Table 25: Comparison of the overall thermal efficiency for receivers 1 and 2 with radiation.

	Tube surface area	Heat flux	Receiver power	Thermal Efficiency
Receiver 1	1.187 m²	356.257 kW	247.121 kW	0.6937
Receiver 2	1.0027 m²	100.265 kW	89.679 kW	0.8941

From the above figures it can be seen that receiver 2 performs overall better then receiver 1, besides for the evaporation efficiency (Table 24). For this process step both receivers generate a greater efficiency then 100 % because the evaporation happens at the lowest temperature level of all three process steps (evaporation, superheating steam and superheating air). Hence a lot of energy from the other processes is transported to and absorbed by the evaporation fluid via radiative and convective heat transfer. It can be observed that the receiver 1 has the lowest efficiency, which is caused by the low heat transfer coefficient of the fluid and the high fluid temperature. It can be considered that these factors cause the high radiation losses from the receiver 1. Receiver 2 has the highest efficiency for superheating air. This is due to the reradiation from the air tube to the steam tube. It can be considered that the steam tube absorbed more energy from the air tube through the radiation exchange.

8.4 Pressure drop

The pressure drop was calculated as described in chapter 2.4.3. The comparison results are shown in Table 26.

Table 26: Comparison of pressure drop for receivers 1-2.

	Superheating air	**Superheating steam**	**Evaporation**
Receiver 1	0.663 kPa	0.544 kPa	0.609 kPa
Receiver 2	14.462 kPa	4.140 kPa	0.459 kPa

From Table 26, it can be seen that receiver 1 can achieve the smallest pressure drop. This is due to the much lower velocity of the fluid flowing through the tubes. Since receiver 2 is using only one tube for each fluid, the velocity will become larger in the same mass flow rate. The results in this section indicate that using the multi-tube is better than using only one helical tube to reduce the pressure drop in the absorber tube.

8.5 Conclusions

Figure 42 shows the conjugated heat losses for receiver 1 and 2 from the Ansys model.
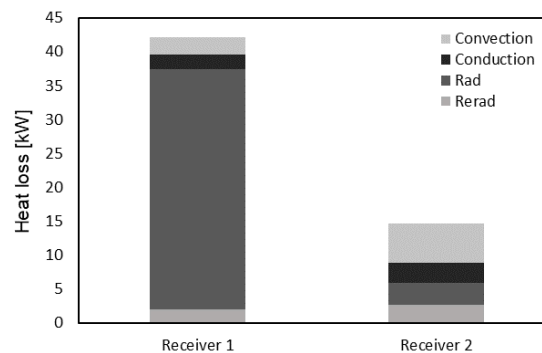
Figure 42: Convection, conduction, radiation and reradiation heat losses for receiver 1 and 2.

It can be seen, that overall receiver 1 exhibits larger heat losses than receiver 2. Receiver 2 exhibits larger re-radiation heat losses and smaller conductive and convective heat losses compared to receiver 1, which matches the results from Lin et al. study [2]. The radiative losses in receiver 1 are more than 90 % higher. The higher radiation losses are caused by the temperature difference. The Inlet air temperature for receiver 1 is 600 °C, whereas receiver 2 is 180 °C. Consequently, there is a temperature difference of 580 K between the inlet of the air and the ambient which causes high radiation losses. Furthermore, this higher inlet temperature

causes an overall increase of the tube wall temperature is for receiver 1 with 991.85 °C compared to receiver 2 with 548.03 °C. Table 27 shows the tube wall temperature for each process step for both receivers.

Table 27: Comparison of tube wall temperature for receivers 1 and 2.

	Superheating air	Superheating steam	Evaporation
Receiver 1	964.89 °C	991.85 °C	397.18 °C
Receiver 2	645.65 °C	548.03 °C	178.09 °C

This, and the fact, that the absorber tube outer surface of receiver 1 is 0.185 m² bigger then receiver 2 ones contributes to the much higher radiation of receiver 1. For the convection, conduction and the reradiation the opposite behaviour occurs. The convection heat transfer of receiver is higher due to the higher heat transfer coefficient and fluid flow velocity of receiver 2 (see Figure 43).
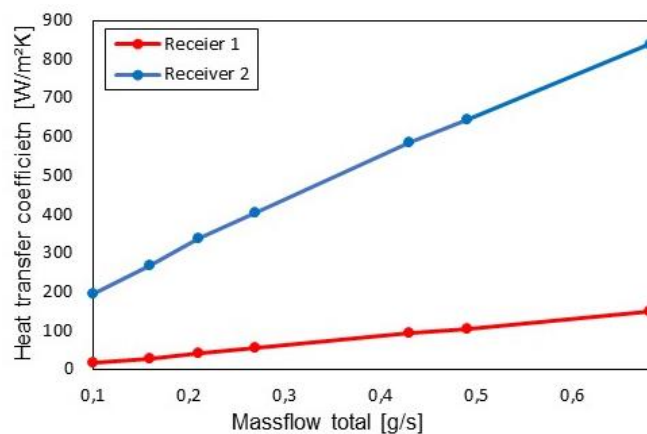
Figure 43: Results receiver 1 and 2 superheating air: heat transfer coefficient vs. total massflow.

It can be seen that receiver 2 reaches overall a higher heat transfer coefficient, compared to receiver one. The total massflow was split onto multiple tubes, which leads to a lower velocity and furthermore a lower heat transfer (see also Figure 44 left). The reradiation of receiver 2 was furthermore higher, because it has a closed backside.

From the calculation it can be seen, that Receiver 1 can achieve the lowest pressure drop. However, the thermal efficiency becomes the lowest when compared to the other receivers due to the high radiation losses. Receiver 2 can achieve the highest thermal efficiency due to much higher heat transfer coefficient. However, the pressure drop becomes much higher compared to receiver 1 due to the much higher fluid velocity. Further enhancing the mass flow rate may

therefore lead to enhanced efficiencies and enhanced pressure drop. From this it is obvious that the flow rat had a significant effect on the thermal efficiency and the pressure drop.

Receiver 1 showed furthermore, that under the geometry conditions in Table 12 it could produce less superheated air then receiver 2. The target outlet temperature for the air of 800 °C could just be reached at a reduced massflow of 100 kg/h.
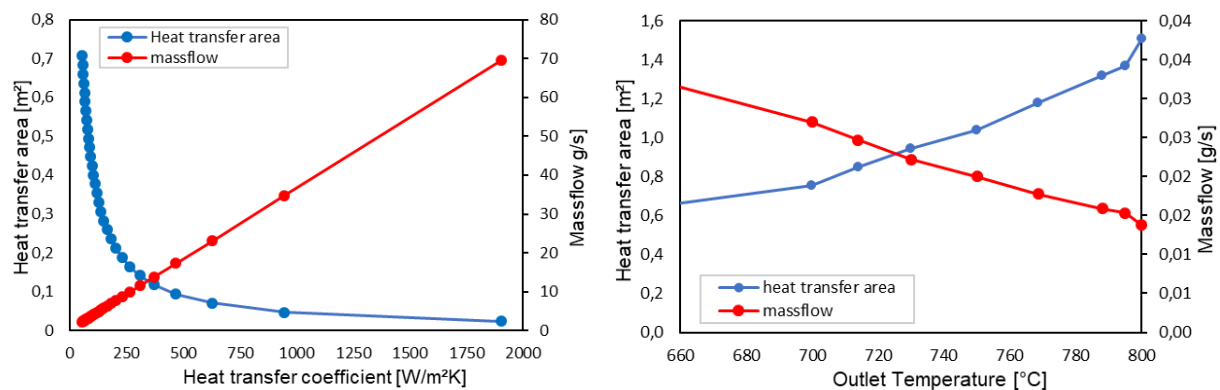

Figure 44: Results receiver 1 superheating air: heat transfer area and massflow per tube vs. heat transfer coefficient (left), Outlet temperature und massflow vs. heat transfer coefficient (right).

Figure 44 shows the correlation between massflow, heat transfer area and the heat transfer coefficient for receiver 1. Both graphs show the same development in the sense that both the heat transfer area and the massflow show an antiproportional behaviour when evaluated to the heat transfer coefficient and the outlet temperature. It is recognisable that, the increasing massflow leads to a higher heat transfer coefficient but to a lower outlet temperature. Whereas a high heat transfer area leads to a lower heat transfer coefficient but to a higher outlet temperature. According to newtons law of cooling it can be assumed, that increasing the heat transfer area is better than increasing the massflow to improve the heat transfer. The same behaviour was examined during simulation tests, where the number of tubes for superheating the air was varied, to increase the outlet temperature to 800 °C at the purposed total massflow of 160kg/h and constant heat flux of 100 kW/m². The results show, that increasing the number of tubes to 32 leads to the target outlet temperature, although the heat transfer coefficient was 81.37 W/m²K. Whereas increasing the heat transfer coefficient to 209.96 W/m²K by using 14 tubes and by that decreasing the heat transfer area, lead to a significant temperature drop to 658.12 °C. Furthermore, at a constant heat flux increasing the surface area leads to a higher amount of energy which can be absorbed. At the same time due to the low velocity a lot of the energy absorbed can be transported to the fluid itself. Though it must be said, that due to the lower temperature difference between fluid and wall and the lower heat transfer area it can be assumed that this aspect can't have a high impact on the total amount of heat transferred.

In this thesis the thermal efficiency and each heat loss mechanism as well as the pressure drop were investigated for two different receiver designs. It can be seen that solar-driven water evaporation, steam superheating and superheating air in a solar receiver is possible and can achieve high efficiencies of 69.37 % and 89.4 1%.

Regarding the pressure drop, receiver 1 showed a better performance. It produces a total pressure drop of 1.82 kPa compared to 19.06 kPa for receiver 2.

Table 28: Comparison of velocity at 10 bars for receivers 1 and 2.

	Superheating air	**Superheating steam**
Receiver 1	3.79 m/s	3.15 m/s
Receiver 2	28.68 m/s	22.40 m/s

From Table 28 the velocity for each process step per tube can be seen. It shows, that receiver 1 has a smaller velocity when compared to receiver 2. The lower velocity causes the much lower pressure drop. The results indicate that using a multi-tube is better than using only one helical tube to reduce the pressure drop in the absorber tube.

9 Summary and Outlook

In this thesis, two solar driven receiver concepts were investigated in a numerical calculation. The simulation was conducted in Ansys steady state thermal analysis. The geometry of both receiver types was constructed in Autodesk Inventor and simulated in a 3D steady-state thermal analysis considering convection, conduction and radiation. The geometry was extended by lines to be used as 1D fluid flow elements to simulate the fluid flow.

The receiver geometry was evaluated in different parametric studies. The impact of the receiver geometry onto the captured radiation was investigated in a raytracing analysis in SPRAY. Three different receiver design were compared and the results show, that the minimum requirement for the aperture opening was 0.2 m. A sensitivity analysis was done in Excel to investigate the effect of the velocity on the pressure drop and the thermal efficiency. The results show that a low velocity and a low number of tubes, leads to a low heat loss and pressure drop. A second parametric study was conducted in Matlab to examine the effect of the tube length onto the heat loss. The analysis showed that the tube should be as short as possible to avoid high thermal losses. The geometry parameters were set using the energy balance.

The model of the receiver was constructed in Ansys steady state thermal. For better meshing, the tubes and the cavity were split in half to generate a homogenous mesh. The tube surfaces and the cavity inner surfaces were modeled with an emissivity of 0.9 and 0.5, respectively. The radiation was considered in the inner cavity wall between backwall, cavity inner wall and the absorber tube outer surface. Since the model is an open cavity the radiative heat exchange also occurs to ambient, which is considered from the backwall and the cavity outer wall.

The water evaporation was investigated in a detailed 1D fluid flow model for the radiative, conductive and convective heat transfer. The 1D two-phase flow model was then coupled to the Ansys steady state analysis. The target for coupling both models was to generate an accurate numerical model at low computational cost and time. The temperature, thermal efficiency, and pressure drop were compared to investigate which receiver performs best. Two different receiver designs were investigated: receiver 1 with straight, connected absorber tubes, cylindrical arranged and receiver 2 with helical, cylindrical absorber tubes. The 1D fluid flow model was validated with different studies and showed a good agreement.

The Ansys model showed a realistic behavior. Both receiver types could provide the target outlet temperature for each step. Though, the massflow for air for receiver 1 had to be reduced to 100 kg/h. For receiver 1 the radiative losses make up for the majority of the heat losses. The

radiation losses were 90 % higher than the radiation losses from receiver 2. This is mainly caused by the higher wall temperature and absorber tube surface area for receiver 1, which leads to higher radiation. Most of the losses from receiver 2 are due to convection. Receiver 2 has a higher velocity which causes higher heat transfer coefficient and consequently a higher heat loss. The results show that overall receiver 2 had a higher thermal efficiency of 89.41 % compared to 69.37 % for receiver 1. Concerning the pressure drop, receiver 1 showed a better performance at a total pressure drop of 1.82 kPa compared to 19.06 kPa for receiver 2. Receiver 1 used a much lower velocity in every tube and could therefore achieve the smallest pressure drop. The results indicate that using multi-tube is better than using only one helical tube to reduce the pressure drop in the absorber tube.

Because both receivers are novel in their temperature level and the cogeneration of superheated steam and air compared to previous developments at DLR, this work can also be used to provide information on up-scaling effects in the development of tubular receivers. The results indicate, that in the upscaling process, a special attention should be placed on the design of the receiver. For receiver 1, due to the splitting of the fluid onto multiple tubes, a small velocity and further a small heat transfer coefficient was one of the main issues. To avoid this the tube inner diameter was drastically decreased to 0.01 m. To still provide enough tube outer surface area to absorb the solar radiation, the tube had to be long (0.75 m). This leads to a continued problem; the cavity diameter was small (due to the small inner tube diameter und the small number of tubes) which caused difficulties in irradiating the whole tube length, because the rays have a step incidence angle. For receiver 2 the problem was the high fluid velocity, because of the small number of tubes (one per process). The high velocity results in a high pressure drop and decrease of heat transferred. To solve this problem, the pressure of the evaporated water, and the superheated air and steam are increased to 10 bars. Because pressurizing air is expensive, splitting the fluid onto more than one tube could provide a cheaper solution to this problem.

As future work, a more accurate model can be achieved by adding the raytracing data to the numerical model to investigate the optical efficiency. Furthermore, as the radiation dominate the heat losses for both receivers, changing the absorber tube coating to decrease the emissivity of the surface can help increase the thermal efficiency (see also 2.3.4). As a result, it can be said, that a low emissivity and high absorptivity of the absorber tube should be targeted.

10 References

[1] Revenkar (2019). Storage and Hybridization of Nuclear Energy, Elsevier. https://doi.org/10.1016/C2017-0-00346-4

[2] Lin et al. (2018). Modeling and design guidelines for direct steam generation solar receiver, Applied Energy 216. https://doi.org/10.1016/j.apenergy.2018.02.044

[3] Ogawa et al. (2007). Hydrogen Production by High Temperature Electrolysis with Nuclear Reactor, Elsevier.

[4] Houaijia et al. (2013). Solar hydrogen by high-temperature electrolysis, SolarPACES. https://doi.org/10.1016/j.egypro.2014.03.208

[5] Monnerie et al. [2018]. Hydrogen production by coupling concentrated solar energy with high temperature steam electrolysis, EHEC.

[6] Schiller *et al*. (2019). Solar heat integrated solid oxide steam electrolysis for highly efficient hydrogen production, Joural of Power Sorces, 416. https://doi.org/10.1016/j.jpowsour.2019.01.059

[7] Schiller et al. (2019).Solid Oxide Steam Electrolysis with Integration of Solar Heat. ECS Transactions, 91. https://doi.org/10.1149/09101.2553

[8] Paitoonsurikarn et al. (2011). Numerical Investigation of Natural Convection Loss From Cavity Receivers in Solar Dish Applications. Journal of Solar Energy Engineering, 133 (2):021004. https://doi.org/10.1115/1.4003582

[9] VDI e.V. (2010). VDI Heat Atlas (2 ed) (8.ed.). Berlin, Heidelberg: Springer. https://doi.org/10.1007/978-3-540-77877-6

[10] Liang Zhao, Liejin Guo, Bofeng Bai, Yucheng Hou, Ximin Zhang. (2003). Convective boiling heat transfer and two-phase flow characteristics inside a small horizontal helically coiled tubing once-through steam generator. *Int. J. Heat Mass Transf.*, 46, 4779-4788. https://doi.org/10.1016/S0017-9310(03)00354-5

[11] J. Buongiorno. (2010). Notes on two-phase flow, boiling heat transfer, and boiling crises in PWRs and BWRs. MIT Department of Nuclear Science and Enginnering. Available online: https://ocw.mit.edu/courses/nuclear-engineering/22-06-engineering-of-nuclear-systems-fall-2010/lectures-and-readings/MIT22_06F10_lec13.pdf [Accessed on July 7, 2021]

[12] S. V. Kadam, M.D. Hambarde (2016). Experimental Study of Heat Transfer Coefficient of Water in Horizontal Tube. International Research Journal of Engineering and Technology (IRJET), 03, Issue 07. https://doi.org/10.4028/www.scientific.net/AMR.505.524

[13] F. W. Dittus, L. M. K. Boelter (1985). Heat transfer in automobile radiators of the tubular type. International communications in heat and mass transfer, Vol. 12, 1. https://doi.org/10.1016/0735-1933(85)90003-X

[14] K. E. Gunger, R. H. Winterton (1989). A general correlation for flow boiling in tubes and annuli. International Jounral Heat Mass Transfer, Vol. 29. https://doi.org/10.1016/0017-9310(86)90205-X

[15] K. Stephan (1992). Heat Transfer in Condensation and Boiling. Berlin, Heidelberg: https://doi.org/10.1007/978-3-642-52457-8Springer

[16] Odeh et al. (1998). Modelling of parabolic through direct steam generation solar collectors. Solar Energy, Vol. 62. https://doi.org/10.1016/S0038-092X(98)00031-0

[17] L. Wojtan, T. Ursenbacher, J. R. Thome (2005). Investigation of flow boiling on horizontal tubes: Part I-A new diabetic two-phase flow. International Journal of Heat and Mass Transfer, Vol. 48. https://doi.org/10.1016/j.ijheatmasstransfer.2004.12.012

[18] B.F. Bai, L.J. Guo. (1997). Study on convective boiling heat transfer in horizontal helically coiled tubes, *Chin. J. Nucl. Sci. Eng.*, 17, 302–308.

[19] L.J. Guo, X.J. Chen, C. Xu, C. Guo, K. Lai. (1998). Forced convection boiling heat transfer

[20] Kyung Won Hwang et al. (2014). Experimental study of flow boiling heat transfer and dryout characteristics at low mass flux in helically-coiled tubes. *Nucl. Eng. Des.*, 273, 529-541. https://doi.org/10.1016/j.nucengdes.2014.03.046

[21] Young-Jong Chung *C*(2014). Boiling heat transfer and dryout in helically coiled tubes under different pressure conditions. *Ann. Nucl. Energy*, 71, 298-303. https://doi.org/10.1016/j.anucene.2014.04.015

[22] Junli Gou et al. (2017). An assessment of heat transfer models of water flow in helically coiled tubes based on selected experimental datasets. *Ann. Nucl. Energy*, 110, 648-667. https://doi.org/10.1016/j.anucene.2017.07.015

[23] Andrew Michael Fsadni, Justin P.M. Whitty. (2016). A review on the two-phase heat transfer characteristics in helically coiled tube heat exchangers. *Int. J. Heat Mass Transf.*, 95, 551-565. https://doi.org/10.1016/j.ijheatmasstransfer.2015.12.034\

[24] Liang Zhao et al. (2003). Convective boiling heat transfer and two-phase flow characteristics inside a small horizontal helically coiled tubing once-through steam generator. *Int. J. Heat Mass Transf.*, 46, 4779-4788. https://doi.org/10.1016/S0017-9310(03)00354-5

[25] Lorenzo Santini et al. (2016). Flow boiling heat transfer in a helically coiled steam generator for nuclear power applications. *Int. J. Heat Mass Transf.*, 92, 91-99. https://doi.org/10.1016/j.ijheatmasstransfer.2015.08.012

[26] Yao Xiao et al. (2018). Experimental investigation of boiling heat transfer in helically coiled tubes at high pressure. *Ann. Nucl. Energy*, 113, 409-419. https://doi.org/10.1016/j.anucene.2017.11.052

[27] ANSYS Inc., ANSYS FLUENT Theory Guide, Canonsbur, PA, 2011.

[28] M. Slootweg (2019). Numerical performance analysis of nocel solar tower receiver. University of Pretoria.

[29] J. R. Howell (1982). A catalog of radiation configuration figures.

[30] T. L. Bergman, F. P. Incropera, D. P. DeWitt (2011). Fundamentals of Heat and Mass Transfer. John Wiley & Sons: Hoboken, NJ, USA.

[31] R. Buck (2021). Solar Power Raytracing Tool SPRAY-User Manual. Deutsches Zentrum für Luft- und Raumfahrt e.V.

[32] C. Förderer (2014). Weiterentwicklung und Validierung eines bestehenden Solarreceiver zur Dampferzeugung. Fachhochschule Köln.

[33] Hempel Holding AG [Online]. https://www.hempel-metals.com/en/material/stainless-steel/314-14841/[Accessed on on August 13, 2021].

[34] Etex Building Performance GmbH [Online]. http://nu-techresources.com/datasheet/PROMAFORMKSen.pdf [Accessed on August 23, 2021]

Appendix

Physical properties stainless steel grade 1.4841 [32]

Parameter	Value
Temperature	20 °C
Density	7900 kg/m³
Specific heat capacity	500 J/kgK
Thermal conductivity	15 W/mK

Physical properties PROMAFORM 1600 [33]

Parameter	Value
Temperature	1600 °C
Density	200 kg/m³
Specific heat capacity	4396.14 J/kgK
Linear shrinkage, 24 hours	1500 °C/ 1.5
Thermal conductivity at mean temperature	
200 °C	0.07 W/mK
400 °C	0.08 W/mK
600 °C	0.10 W/mK
800 °C	0.13 W/mK
1000 °C	0.18 W/mK

Eidesstattliche Erklärung

Ich erkläre hiermit, dass ich die vorliegende Arbeit ohne unzulässige Hilfe Dritter und ohne Benutzung anderer als der angegebenen Hilfsmittel angefertigt habe; die aus fremden Quellen direkt oder indirekt übernommenen Gedanken sind als solche kenntlich gemacht. Der von mir erbrachte Anteil im Rahmen einer Gruppenarbeit ist eindeutig gekennzeichnet.

Insbesondere habe ich nicht die Hilfe einer kommerziellen Beratung in Anspruch genommen. Dritte haben von mir weder unmittelbar noch mittelbar geldwerte Leistungen für Tätigkeit erhalten, die im Zusammenhang mit dem Inhalt der vorgelegten Arbeit stehen.

Die Arbeit wurde bisher weder im Inland noch im Ausland in gleicher oder ähnlicher Form eingereicht und ist als Ganzes noch nicht veröffentlicht.

Erfurt, den 27. August 2021